Nonlinear and Plastic Behavior of Soft Thermoplastic and Filled Elastomers Studied by Dissipative Particle Dynamics

Didier Long* and Paul Sotta†

Laboratoire de Physique des Solides, Université de Paris XI/CNRS, Bât. 510, 91405 Orsay Cédex, France

Received June 12, 2006; Revised Manuscript Received July 11, 2006

ABSTRACT: We propose here a model for describing mesoscale relaxation mechanisms in soft thermoplastic elastomers, and also in the high-temperature regime of filled rubbers. The model is solved by dissipative particle dynamics. We study the response of these systems to deformations of various amplitudes and show that the systems exhibit plastic behavior. We characterize the elastic and plastic regimes of deformation. We show that the plastic behavior is related to irreversible reorganizations at a mesoscopic scale. We characterize the latter as buckling of instabilities that change the local environment of the hard inclusions. We study the effect of filler volume fraction and of the elastic disorder. Though the mechanisms described here are not the only possible source of plasticity in these systems, they might be relevant in many circumstances.

1. Introduction

Composite polymeric materials have an extremely wide range of applications. They are used to make tires (reinforced or filled elastomers), damping materials, shock absorbers,[1−3] and medical prostheses.[4] Thin films are used in electronics applications.[5] In view of the particular application, their properties can be optimized according to various criteria. For some applications such as reinforced rubbers, a very high resistance to tear and wear is required.[3,6−8] For biomedical or mechanical applications, they must have a high resistance to fatigue and, specifically, retain their initial shape even after a large number of deformation cycles.[4,9−25] The progress in chemical synthesis and engineering has allowed for the designing of very diverse nanostructured materials, such as those made of block copolymers, to obtain materials with tailored physical and mechanical properties.[26−29]

Thermoplastics elastomers are a wide class of such systems and are made of, e.g., block copolymers such as ABA or ABC triblocks. They can be processed in a melt state at high temperature and become structured materials at room temperature without needing costly processes such as vulcanization. Copolymers exhibit a great diversity of microphase structures. We are interested here in the so-called spherical morphologies, with spheres of A or C polymers embedded in a continuous matrix of B polymers. These systems are particularly important when the A and C polymers are in the glassy state at room temperature, whereas the B polymer has a low glass-transition temperature and is in the rubbery state at room temperature. In the spherical morphology, these systems behave as rubbers over a wide temperature range. The glassy spheres act as cross-links. Such systems can be obtained with polystyrene-*block*-isoprene-*block*-polystyrene triblock copolymers (PS-*b*-PI-*b*-PS), PS-*b*-PB-*b*-PS (PB: polybutadiene), or PS-*b*-PB-*b*-PMMA (PMMA: poly(methyl methacrylate)). Other thermoplastics can be obtained by so-called graft copolymers[26] made of a rubbery backbone with several grafted lateral chains of high-T_g polymers. It is then possible to obtain systems made of glassy units embedded in a rubbery matrix with a glassy volume fraction up to 40%. The observed morphologies depend on the volume fraction of each component, the degree of incompatibility of the various blocks, on the molecular architecture, and also on the methods of preparation as well. A high shear rate in the melt state may favor dispersion of one phase in the other, especially after rapid cooling of the sample. The morphology depends also on the history of the sample. For instance, in ABC triblock copolymer samples, one can obtain a morphology of hard cylinders of, e.g., 60% volume fraction or more, embedded in a rubbery matrix. Such samples often have a high Young's modulus and exhibit a yield behavior at small deformation, which can be interpreted as the consequence of the breaking of the glassy cylinders. When subsequently deformed, they behave as soft thermoplastic elastomers without a yield point.[21,30] The morphology then corresponds to a dispersion of hard beads in a rubbery continuous matrix. Cylinder breaking is indeed an irreversible process at room temperature. Therefore, dispersions of glassy or hard polymer beads in a rubbery matrix correspond to very diverse situations covering a wide range of volume fraction. In this work, we aim at studying the elastic and plastic properties of thermoplastic elastomers made of a disperse hard phase embedded in a rubbery matrix. The volume fraction of glassy beads will be between 20 and 45%. In practice, these systems cover a wide range of elastic properties, with a shear modulus ranging from 10^4 Pa to 10^7 or 10^8 Pa.[26]

When dealing with the elastic properties of these systems, theoretical models are faced with a number of difficulties of varying nature. First of all, the microscopic mechanisms at the origin of macroscopic elasticity in disordered systems,[31] and specifically in systems such as gels or rubbers,[32−36] is not yet completely understood. Gels or rubbers are made of cross-linked networks of polymer chains. When deforming a sample, the strands between cross-links are stretched, which results in a decrease of entropy and thus in a free energy cost. This entropic origin of the elastic properties of gels or rubbers is no longer disputed. However, a precise, microscopic description of the strand network deformation under shear has long been elusive. Classical models developed in the polymer literature for describing rubber elasticity have assumed affine deformation down to the strand scale. On the other hand, it has long been known that this hypothesis is not correct.[34,35,37−40] To go beyond this assumption, some authors have proposed that the sol−gel

* Corresponding author. E-mail: D. Long: long@lps.u-psud.fr.
† E-mail: sotta@lps.u-psud.fr.

10.1021/ma061306e CCC: $33.50
Published on Web 08/09/2006

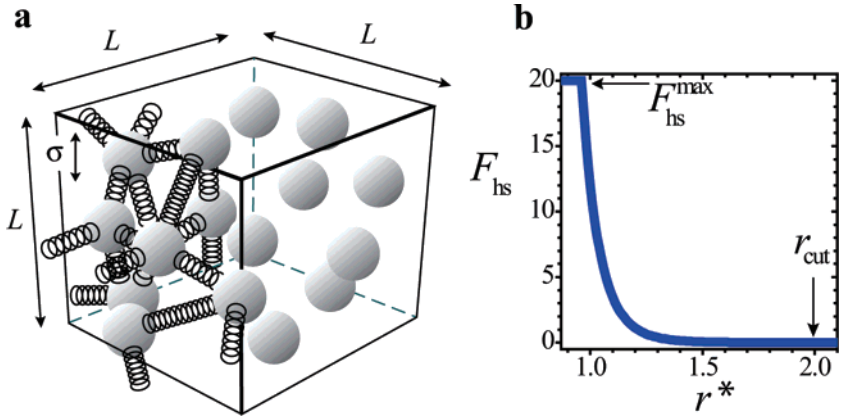

Figure 1. (a) Schematics of the model. For clarity, only a fraction of the springs have been drawn. Filler particles are connected by elastic springs and interact via a hard-core potential at short distances. The corresponding hard-core force is plotted in (b) as a function of the reduced distance $r^* = r/d$, where d is the particle diameter.

transition is analogous to percolation.[41−46] More recently the question of the nonaffine nature of the displacements on small scales has been addressed in gels.[47−50] Another important feature is the role played by excluded volume[51,52] and also by entanglements. Indeed, it has been demonstrated that entanglements are essential for understanding the sol−gel transition and also for explaining the observed value of the shear modulus, especially in the case of very long chains.[53−56] A further difficulty in describing gel or rubber elasticity is that these systems are intrinsically disordered and inhomogeneous as a result of their preparation.[57,58] Cross-linking not only freezes in the disorder present in the melt but also tends to enhance it; the more a region is cross-linked, the more it tends to collapse, which in turn enhances further cross-linking in this region. This results in large-scale heterogeneities that are responsible for turbidity in gels, for instance, and which have been evidenced experimentally.[34,59]

The presence of the hard beads embedded in a rubbery matrix is expected to create specific features. First, the glassy beads are an important source of elastic disorder on a scale larger than that of the cross-linking process in pure rubbers. At small deformation, the glassy spheres should in principle favor affine deformation because they cannot cross each other. On the other hand, at larger deformations, the relative positions of the hard spheres may be modified in an irreversible way. Thus, the presence of the glassy spheres results in a very complex pattern of free energy barriers that can be modified irreversibly by an imposed deformation. This may result in plastic deformation, as well as hysteresis in internal properties such as the free energy, during an imposed deformation cycle. We propose a model for describing such elastic and plastic properties of thermoplastic elastomers. The scale of interest here is larger than the distance between cross-links or entanglements usually considered in gels or rubbers. It is typically on the order of 10 nm, which corresponds to the diameter of the glassy beads. The purpose of this work is to describe the mesoscale behavior of such a system when submitted to imposed deformations. We study both static and dynamical properties by dissipative particle dynamics. We aim at characterizing the onset of nonlinear behavior and plasticity in relation to the disordered nature of the microscopic deformations. Our approach should also be of interest for describing elastic and plastic properties of filled elastomers in the high-temperature regime. In filled elastomers, the presence of filler particles introduces additional issues. An important feature is the shift of the glass-transition temperature induced by the presence of the fillers. Indeed, it has long been proposed that the polymer matrix in the vicinity of the filler is glassy.[60−64] More recently, Montes, Lequeux, and co-workers have shown that this glassy layer plays an essential role in the reinforcement mechanism.[65−67] On the other hand, at a relatively high temperature, the glassy layer is too thin to play an important role, and the reinforcement is prominently due to the steric effects of the fillers.[65−67] Our work here could be applied for describing elastic and plastic properties of such systems.

Given the very wide spatial and temporal scales involved in the physics of thermoplastic and/or filled elastomers, it is a daunting if not impossible task to address all the issues mentioned above in a single picture. Depending on the issues of interest, one must primarily focus on some particular aspect of the physics of these systems.

Among recent related works, the finite element mapping with spring network representations by Gusev has to be mentioned.[68] This model is suitable to describe elastically inhomogeneous materials. However, the dynamical behavior and large deformations have not been investigated within this framework. DiDonna and Lubensky[49] have also shown that deformations are nonaffine in random elastic networks. Their study was performed by minimizing a free energy function and is thus inadequate for studying large, irreversible deformations such as those discussed here. More specifically, regarding filled elastomers, Starr and Glotzer have developed an approach based on molecular dynamic simulations for describing reinforcement properties of filled elastomers.[69] However, their approach is based on simulations down to the molecular scale and cannot reach both the space and time scales of interest here.

The paper is organized as follows. In Section 2, we describe the basic features of our model. In Section 3, we introduce basic definitions of physical quantities and show how the dynamics of our system is solved by numerical simulations. In Section 4, we consider first the linear regime of deformation and the onset of the nonlinear regime (Section 4A). Then (Section 4B), we characterize the nonaffinity of the displacements at large deformation amplitudes as a function of various parameters such as the filler volume fraction, the stiffness of the rubber matrix, and the amplitude of the deformation. In Section 4C, we describe the plastic properties of our systems, which we relate to microscopic instabilities (buckling) in Section 4D.

2. Description of the Model

The basic ingredients we want to implement in the simulated system are permanent elasticity, disorder, and excluded volume effects. The model is depicted in Figure 1. The dispersion of glassy or hard beads is represented by hard spheres of diameter

d randomly distributed in space. The hard sphere potential is described by:

$$V_{hs}(r^*) = \begin{bmatrix} F_{hs}^{max} r^* + H & (r^* < r_{min}) \\ \epsilon^* r^{*-12} & (r_{min} < r^* < r_{cut}) \\ 0 & (r_{cut} < r^*) \end{bmatrix} \quad (1)$$

where $r^* = r/d$ is the reduced dimensionless distance between particles. Though we will keep it in our notations, d should be considered to be the length scale of the problem and takes the value 1. The parameter $\epsilon^* = 1$ determines the energy scale in the system. The force F_{hs} cancels at a cutoff distance $r_{cut} = 2$. At this distance, F_{hs} is already much smaller than ϵ^*. The force F_{hs} is limited to F_{hs}^{max} at short distances to prevent numerical instabilities in the initial step of the simulations, in which the centers of two particles may be very close. The constant H is chosen to ensure the continuity of the potential. The force $F_{hs}(r^*)$ rises very sharply at r^* of the order one. For instance, it is already of the order 20 (in units of ϵ^*) for $r^* \approx 0.96$. This means that it is indeed quite realistic to consider d as the particle diameter.

To model the effect of the disordered rubbery matrix, the particle centers are connected to their closest neighbors by an average number n of harmonic springs. The corresponding elastic interaction potential is given by:

$$V_{el}(r^*) = \frac{k^*}{2}\left(\frac{r^*}{l^*_0} - 1\right)^2 \quad (2)$$

where $k^* = kd^2 l_0^2/\epsilon^*$ is the reduced spring stiffness (in units of ϵ^*) and l_0^* is the reduced equilibrium length of the springs (in units of d). Thus, the particles interact both with a hard-core repulsion and elastic springs.

Periodic boundary conditions are used in order to simulate bulklike behavior. To prepare the system, N particles are dispersed at random in a box of volume $V = L^3$, such that the volume fraction takes the chosen value Φ. The box volume V is kept constant throughout the simulations. For an average number of connections per particle n, the total number of springs in the system is $Nn/2$ (one spring contributes to two connections). The $Nn/2$ closest particle pairs are connected by springs. The length l_0^* is set equal to the average distance between neighboring sites on an ordered simple cubic lattice, that is, $l_0 = (1/n)(6 + (n - 6)\sqrt{2})a$ (for $6 < n < 18$), where a is the lattice parameter corresponding to the volume fraction Φ, given by $a^3 = \pi/6\Phi$. This value for l_0 is quite arbitrary, but the properties of the systems that will be investigated do not depend on this particular choice. Thus, the parameters that are relevant for describing our samples are the volume fraction Φ of the solid particles and the degree of connectivity n.

We assume that the degrees of freedom, which are the centers of mass of the hard spheres, move relative to each other with a friction coefficient ζ. The hydrodynamic friction is computed within a mean field approximation:

$$\vec{F}_{Hydro} = -\zeta^*(\vec{v}^* - \langle\vec{v}^*\rangle) \quad (3)$$

where $\zeta^* = \xi d^2/\epsilon^* = 1$ is the reduced friction coefficient, which has the dimension of time and thus sets the time scale in the system. $\vec{v}^*$ is the reduced velocity of a particle, and $\langle\vec{v}^*\rangle$ the average reduced velocity of the surrounding particles (reduced velocities have the dimension of an inverse time). To save computational time, the hydrodynamic friction is computed with respect to the average affine deformation rate rather than to the actual motion of the particle surrounding.

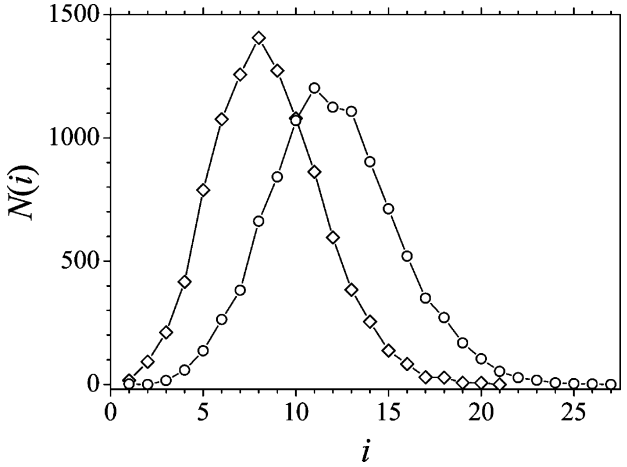

Figure 2. One main source of disorder in the system is the distribution of connectivities, i.e., the number of springs connected to each particle. $N(i)$ is the number of sites with a connectivity i in systems with $N = 10^4$ particles: (◇) average connectivity $n = 8.5$; (○) $n = 12$.

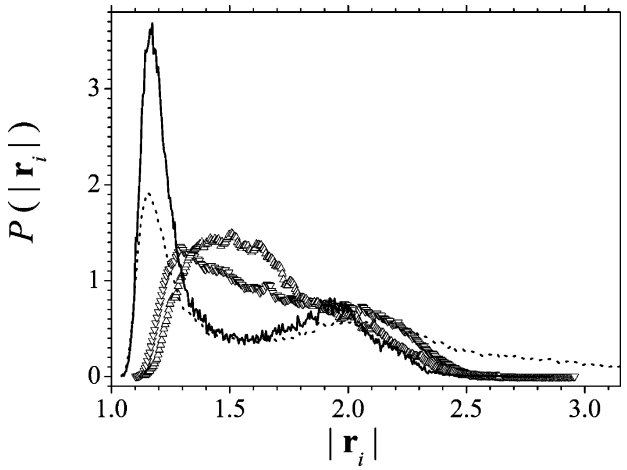

Figure 3. Distribution of bond (spring) lengths in the initial, equilibrium state: plain curve: $\Phi = 0.40$, $n = 12$; (△) $\Phi = 0.20$, $n = 12$; (▽) $\Phi = 0.20$, $n = 8.5$. The dotted curve is the distribution in the system $\Phi = 0.40$, $n = 12$, at a shear deformation of amplitude $\gamma_{max} = 2.0$, which shows that the system does not crystallize under shear. The probability densities for a given bond to have a length r_i are plotted here, with a resolution $\Delta r = 0.005$.

In this system, the disorder is introduced by the dispersion of the connectivity number around the average value, and also by the fact that spheres are connected not only to closest neighbors, but also to some other spheres beyond the first neighboring shell. This results in a distribution of distances r^*, and thus in a distribution of elastic forces. An example of a histogram of connectivity is given in Figure 2. This kind of elastic disorder is sufficient for ensuring that the dispersion of the spheres is disordered at equilibrium (see Figure 3). Equivalently, one may consider that all spheres have the same number m of springs but that the elastic constant takes randomly a value 0 or 1. A generalization of this model could be obtained by allowing the elastic spring constants to follow any continuous distribution. The model system considered here includes potentials that depend on the distances between particles only, without bending energies. Because we aim at representing systems with a strong elastic behavior (i.e., far from being floppy), we shall only consider relatively large values of the connectivity n.[43−46] Our simulations show that, without hard sphere inclusions ($\Phi = 0$), values of n larger than 8 lead to

samples with a shear modulus of order one, corresponding thereby to the regime of interest here. Let us emphasize again that the elastic springs in our model represent the elastic interaction between hard beads due to the elasticity of the rubbery matrix as a whole, not the actual number of polymer strands between them, because we consider the system at the scale of the distance between glassy beads, which is larger than distances between cross-links and/or entanglements.

3. Solving the Model

In this section, we introduce basic concepts and definitions regarding the physical quantities of interest. We describe how the dynamics is solved and how various quantities, such as shear moduli or plastic behavior, are computed.

3A. Dissipative Particle Dynamics. At the considered spatial scales and frequencies, the equations of the dissipative molecular dynamics are noninertial.[70] They include a source of dissipation in the form of a hydrodynamic friction term. At the scale of the fillers, thermal noise is negligible. The equation of motion for particle i is thus:

$$\vec{F}^i_{\mathrm{el}} + \vec{F}^i_{\mathrm{hs}} + \vec{F}^i_{\mathrm{Hydro}} = 0 \tag{4}$$

which gives the velocities at time t as a function of the positions $\vec{r}^{\mathrm{i}}$, within the mean field approximation (see eq 3):

$$\vec{v}^{\,i} = \langle \vec{v} \rangle + \frac{1}{\zeta}[\vec{F}^i_{\mathrm{el}} + \vec{F}^i_{\mathrm{hs}}] \tag{5}$$

The positions and velocities are computed every time interval dt. The equations of motion are solved using the modified midpoint method (MMM).[71] dt is subdivided in p time intervals ddt (such that $dt = pddt$). The velocities and new positions of all particles are computed at each time step ddt, while the velocities are considered to be physically significant at the end of the dt time interval only. In the simulations, the time scale is fixed by the value of the reduced friction coefficient $\zeta^* = 1$. This time scale corresponds to the typical relaxation time of a particle. The relaxation times measured in the system should thus be compared to this time scale. Unless explicitly specified, times will be expressed in units of ζ^*, denoted "sec". In real systems, the elementary time scale is determined by the rubber matrix behavior. Note that real rubbers often do not exhibit exponential relaxation but display slower relaxations often described as power laws, especially when they are loosely cross-linked.[32,72] We assume that the rubber matrix corresponds to an ideal highly cross-linked rubber, which might well be described by a single relaxation time corresponding to the so-called Rouse relaxation time.[32,70]

3B. Deformation of an Isotropic Solid. *Virial Stress Formulation.* In an elastic isotropic body and for small deformations, the stress tensor $\sigma_{\alpha\beta}$ is related to the strain tensor $\mathbf{u}_{ij}$ by the constitutive equation:

$$\sigma_{\alpha\beta} = K\delta_{\alpha\beta}u_{ll} + 2\mu\left(u_{\alpha\beta} - \frac{1}{3}\delta_{\alpha\beta}u_{ll}\right) \tag{6}$$

where summation of elements with repeated indices is implicit. K is the bulk (compression) modulus and μ the shear modulus.[73] Consider a box of volume V^* containing N particles. The stress tensor is related to the forces exerted on the particles by the Kramers Kirkwood formula, which provides a microscopic expression for the stress tensor:[70]

$$\sigma_{\alpha\beta} = -\frac{1}{V^*}\sum_i F^i_\alpha R^i_\beta \tag{7}$$

where F^i_α is the α component of the sum of the forces exerted on particle i by other particles *in the considered sample* and R^i_β is the β-component of the position of particle i. The stress tensor is symmetric by construction. Periodic boundary conditions in the simulation box ensures that:

$$\sum_i F^i_\alpha = 0 \tag{8}$$

Also, the periodic boundary conditions and the fact that we consider only central forces ensure that the total torque applied on the sample cancels (see Appendix, Part A):

$$\vec{T} = \sum_i \vec{R}^i \wedge \vec{F}^i = 0 \tag{9}$$

3C. Preparation of the System. The purpose of the preparation steps is to obtain an equilibrated sample in which the total force acting on each particle is zero and the stress tensor is isotropic. Immediately after the particles have been randomly distributed, none of these conditions is satisfied. For instance, many of the filler particles overlap, and they are thus submitted to strong, not equilibrated repulsive forces. We must therefore let the sample equilibrate by first canceling the forces (or velocities) on each particle, and then canceling the nonisotropic part of the stress tensor.

1. First Initialization Step. This first step consists of canceling the particle velocities or, equivalently, the potential forces exerted on each particle. The box shape is maintained constant throughout this relaxation step. The time resolution ddt chosen to solve the equations of motion must obey $vddt \ll r_0$, where v is the particle velocity and r_0 the typical interparticle distance. The initial velocity may be of the order 10−100, which imposes $ddt \approx 10^{-4}$ with $r_0 \sim 0.1$. We have chosen $dt = 10^{-3}$ and $p = 10$ typically, which gives $ddt = dt/p = 10^{-4}$. In this step, the system is relaxed typically during 0.2−0.4 time units (sec), which corresponds to 200−400 dt steps. At the end of this first step, the average velocity is not rigorously zero, but has dropped to a value of the order unity at most.

2. Second Initialization Step. In an infinite system, the stress tensor σ immediately after the particles have been distributed randomly should be isotropic:

$$\sigma = -PI_{\mathrm{d}} \tag{10}$$

where P is the pressure and I_{d} the identity tensor. In a finite simulation box, $\sigma_{\alpha\beta}$ is of the form

$$\sigma = -PI_{\mathrm{d}} + \tilde{\sigma} \tag{11}$$

where the nonisotropic part $\tilde{\sigma}_{\alpha\beta}$ (deviatoric stress tensor) is a traceless tensor. One can show (see Appendix, Part B) that the deviatoric stress tensor elements $\tilde{\sigma}_{\alpha\beta}$ scale like $N^{-1/3}$ after the particles have been randomly distributed, and at the end of the first relaxation step as well. Therefore, in a sample of 10^4 particles, this tensor is of order 0.1 and cannot be neglected as compared to the pressure, which is of order 1.

Thus, to obtain a reference state with isotropic stress tensor, the sample must be deformed so as to cancel the deviatoric of the stress tensor $\tilde{\sigma}$. It is important to notice that the elements $\tilde{\sigma}_{\alpha\beta}$ must be canceled with a high degree of precision (typically better than 10^{-5}), so that the mechanical response (such as the shear modulus) can be measured with a good accuracy. Note

also that all deformations are performed at constant volume in order to model the behavior of real rubbers, whose bulk modulus is very large compared to the shear modulus. To cancel $\tilde{\sigma}$, the following iterative deformation process is used. At a given step t, a small deformation tensor $I_d + d\Gamma$ is applied so that the new deformation tensor at time $t + dt$ becomes

$$\Gamma(t + dt) = \frac{(I_d + d\Gamma)\Gamma(t)}{[\det(I_d + d\Gamma)]^{1/3}} \tag{12}$$

The infinitesimal deformation $d\Gamma$ is defined by

$$I_d + d\Gamma = I_d - C\tilde{\sigma} \tag{13}$$

with $\tilde{\sigma}_{\alpha\beta} = \sigma_{\alpha\beta} + P\delta_{\alpha\beta}$, where the pressure P is computed as $P = -\mathrm{Tr}\ \sigma/3$. After applying the deformation $I_d + d\Gamma$, the system relaxes during a time interval Δt. The stress is then measured and the process iterated. C is a positive number whose value must be chosen to ensure that the spheres do not overlap too much during each relaxation step described by eq 12 and also has to be optimized so that the simulation of the relaxation is as fast as possible. This procedure is iterated until all components of $\tilde{\sigma}_{\alpha\beta}$ are zero to the prescribed precision. Before starting the proper numerical experiments, the samples are submitted to a few (typically 6−10) high-amplitude elongation cycles (up to $\lambda = L/L_0 = 2$ typically) in order to remove internal instabilities (bucklings), thereby reducing the dispersion in the results. Finally, after performing these preliminary cycles, the second step (iterative deformation process) is performed again to cancel the residual stress, until the nonisotropic elements of the stress are smaller than 10^{-5} typically.

3D. The Shear Experiment. After obtaining an equilibrated system along the lines described above, various experiments may be performed. The shear experiments may be performed at any time-dependent rate. An oscillatory shear may be applied at various amplitudes and frequencies (Section 4A). The main results presented in this paper (Section 4B−D) concern shear cycles which are performed in the following way. The system is first sheared up to a maximum shear value γ_{max} at a constant shear rate $\dot{\gamma}$ (state (I) in Figure 4). This is achieved by applying successive small shear steps $d\gamma$ described by the deformation tensor (see Figure 4):

$$I_d + d\Gamma = \begin{bmatrix} 1 & d\gamma & 0 \\ 0 & 1 & 0 \\ 0 & 0 & 1 \end{bmatrix} \tag{14}$$

At each elementary step $d\gamma$, the system is first affinely deformed and then relaxes during a time interval Δt, such that the shear rate $\dot{\gamma} = d\gamma/\Delta t$. After reaching γ_{max}, we let the system come back to a new equilibrium state at isotropic stress (state (II) in Figure 4), thus achieving a large-amplitude shear cycle. The way back to equilibrium is achieved with the same procedure as in the second initialization step, described in Section 3C. To relax the applied stress, small iterative deformations of the form $d\Gamma_{\alpha\beta} = -C\tilde{\sigma}_{\alpha\beta}$ with $\tilde{\sigma}_{\alpha\beta} = \sigma_{\alpha\beta} - P\delta_{\alpha\beta}$ are applied. At each relaxation step, a small rotation must be applied to preserve the pure shear symmetry of the strain tensor. This will be described in more detail in Section 4C. Alternatively, we may also let the stress relax as a function of time while maintaining the system at the imposed shear deformation γ_{max}.[50]

3E. Simulation Times. All the results presented here have been obtained with systems which contain $N = 10^4$ particles. That corresponds to a simulation box of about $21 \times 21 \times 21$ particles, that is, a box volume $24.2 \times 24.2 \times 24.2$ (for $\Phi = 0.37$) to $29.7 \times 29.7 \times 29.7$ (for $\Phi = 0.20$). This size has been chosen to obtain reasonable simulation times. For this size, the performance of the machine corresponds roughly to 25−40 s (in terms of system unit time) per 1 h computer time (depending on the connectivity n). The duration of the simulations depends on the time (in sec) over which the system is studied, or more precisely on the number of time steps dt, which is typically $dt = 0.02$. To achieve a high amplitude shear cycle, the following steps must be performed: velocity and stress relaxation (3000 dt steps typically), initial elongation cycles (15 000 dt steps), stress relaxation (60 000 dt steps), shearing up to $\gamma_{max} \approx 2$ at $\dot{\gamma} = 0.1$ (1000 dt steps), relaxation to zero stress (up to 50 000 dt steps), or alternatively long time relaxation of the stress at constant γ_{max} (up to 50 000 dt steps). Oscillatory measurements at low frequencies are also time-consuming. Thus, each shear cycle performed on a new system typically corresponds to 120 000−130 000 steps dt, or equivalently 2400 s in terms of system unit time (sec). The simulations have been performed on a cluster of four XEON biprocessor machines operating at 2.4 GHz. This gives an overall duration of the whole experiment of the order of 60−100 hours computer time. On the other hand, performing an experiment (stress relaxation under large-amplitude shear, for example) on a system already prepared corresponds to about 30 computer time hours. The results of about 30 different systems (4 values of the connectivity n and 8 values of the volume fraction Φ) are presented here. In each system, the relaxation back to zero shear was studied for typically 6−8 values of the shear amplitude γ_{max}, from 0.02 to 2.4. Typically, two samples of each systems have been generated. All together, this corresponds roughly to 2×10^4 hours computer time.

4. Results and Discussion

The results presented here are mainly focused on the description of the plastic properties of the systems and on the way they are related to the disordered nature of the microscopic motions of the hard inclusions. Thus, we will study two main aspects: the nonaffinity of the microscopic displacements and the residual deformation of the samples after the external stress has been suppressed and the system has relaxed for a long time. The main parameters that we consider are the volume fraction Φ, which has been varied between 0.20 and 0.42, and the connectivity n ($n = 8.5$ to $n = 12$) which is related to the stiffness of the rubbery matrix. First, we characterize the linear regime of deformation and the onset of the nonlinear behavior.

4A. Complex Shear Modulus. *Onset of the Nonlinear Regime.* The dynamical response of the systems, that is, the frequency-dependent complex modulus, has been measured for various strain amplitudes. An oscillatory shear strain of the form $\gamma(t) = \gamma_0 \sin \omega t$ is applied, starting from $t = 0$, with an integer number of strain increments per period (from 8 to 256 depending on the amplitude γ_0), and the stress $\sigma_{xy}(t)$ is measured. After a time 25−50 s, a permanent regime is observed. Both the strain and stress are Fourier transformed over an integer number of periods (from 1 to 64 according to the frequency), and the complex modulus $G'(\omega)$ (respectively $G''(\omega)$) is obtained as the ratio of the in-phase (respectively out-of-phase) Fourier component of the stress to the Fourier component of the strain at frequency ω. Note that the shear modulus μ defined in eq 6 is related to the frequency-dependent complex modulus $G(\omega) = G'(\omega) + iG''(\omega)$ by the relation $\mu = G'(\omega = 0)$.[32,70] Figure 5 shows the oscillatory shear modulus G' measured at an amplitude $\gamma \approx 0.03$ and frequency $\omega/2\pi = 0.625\ s^{-1}$, as a function of the volume fraction Φ for different values of the connectivity n. This graph illustrates the reinforcement mech-

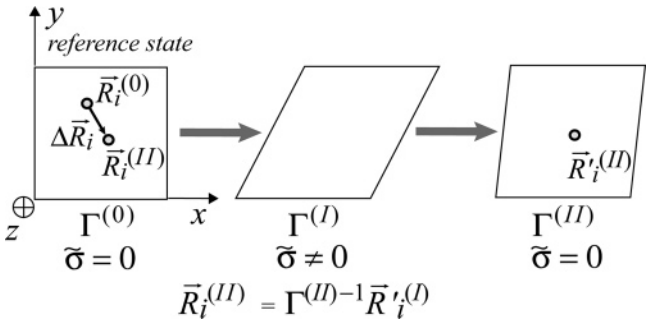

Figure 4. Schematics illustrating the symmetry of the applied shear. In the reference state (0), the strain tensor is $\Gamma^{(0)} = I_d$ and the anisotropic part of the stress tensor is $\tilde{\sigma} = 0$. The applied shear is characterized by the nonzero element γ_{xy}. In state (II), the system has returned to zero anisotropic stress and relaxed for a long time. The definition of the nonaffine displacement vectors in state (II), referred to the initial undeformed state, is schematized as well.

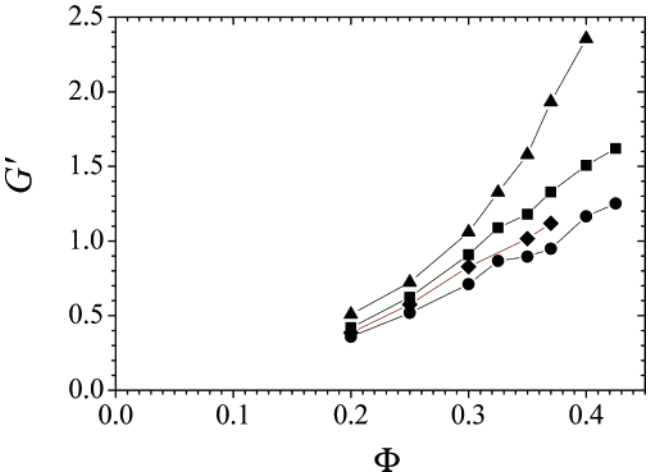

Figure 5. Oscillatory shear modulus, measured at an amplitude $\gamma = 0.03$ and frequency $\omega/2\pi = 0.625\ s^{-1}$ as a function of the volume fraction Φ, for different values of the connectivity: (■) $n = 10$; (♦) $n = 9$; (●) $n = 8.5$; (▲) $n = 12$. The shear modulus is measured by Fourier transforming the strain and stress over 32 periods after waiting 8 periods after the beginning of the shear.

anism due to an increasing fraction of hard inclusions. These results may be compared, e.g., to those in refs 65 and 66, in which the shear moduli were measured in poly(ethylacrylate) matrixes filled with silica particles as a function of the frequency, temperature, and particle volume fraction. In the high-temperature regime ($T \gtrsim T_g + 100$ K typically), at a given (low) frequency, it was found that the modulus increases by a factor of about 4 as the volume fraction increases from about 8% to about 20%. Thus, the results presented in Figure 5 may be considered to be in qualitative agreement with these observations. On increasing the amplitude of the deformation, a decrease of the modulus G' is observed.[50] The amplitude $\gamma \approx 0.03$ can be considered as the onset of the nonlinear regime.

4B. Nonaffine Displacements. As mentioned above, most rheological models assume that the deformations are affine down to the molecular scale.[32,33,70] Whereas this assumption has provided a useful way of describing, e.g., polymer melt dynamics, it has proven wrong and misleading in the case of systems with frozen disorder, such as gels or rubbers. We aim here at quantifying the nonaffine part of the displacements, down to the scale of the filler particles. To quantify the deviation with respect to affine deformation, we proceed as follows. The displacements of all particles are computed with respect to the initial equilibrium state obtained after the full preparation process (reference state (0)), characterized by the deformation tensor

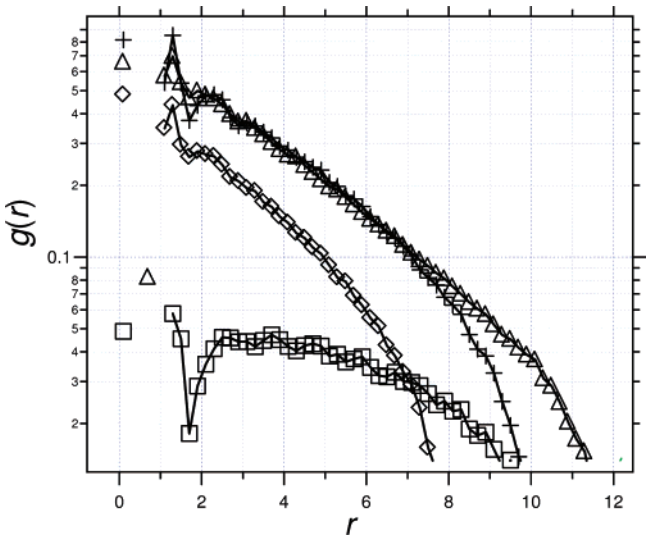

Figure 6. Correlation function of nonaffine displacements after a cycle of large amplitude shear in the system $n = 10$, $\Phi = 0.37$. r is the distance between correlated particles, the correlation function is averaged isotropically on r. (△) $g_{yy}(r)$; (+) $g_{xx}(r)$; (◇) $g_{zz}(r)$; (□) $g_{xy}(r)$. $n = 8.5$, $\Phi = 0.35$, $\dot{\gamma} = 0.1$, $\gamma_{max} = 1.88$.

$\Gamma^{(0)} = I_d$. In the initial state (0), the particle i is located at position $\vec{R}_{i(0)}$. A second state (I) is obtained, for instance, after the system has been deformed up to a deformation state described by the tensor $\Gamma^{(I)}$. At a given time, the position of particle i in state (I) is $\vec{R}_i'^{(I)}$. This position can be associated to the position $\vec{R}_i^{(I)}$ in the reference system, defined by $\vec{R}_i'^{(I)} = \Gamma^{(I)}\vec{R}_i^{(I)}$. Thus, the nonaffine displacement of particle i considered in the reference system (0) is

$$\Delta\vec{R}_i = \vec{R}_i^{(I)} - \vec{R}_i^{(0)} \tag{15}$$

This is illustrated in Figure 4. Then the nonaffinity may be quantified by the histograms of the coordinates of the nonaffine displacements $\Delta\vec{R}_i$, or of the modulus of this vector. Correlation functions for the nonaffine part of the displacement may also be defined as

$$g_{\alpha\beta}(\vec{r}) = \langle \Delta R_{i\alpha} \Delta R_{j\beta} \rangle \tag{16}$$

where $\alpha,\beta = x, y, z$ and the average is done over all particle pairs (i, j) with an interparticle vector $\vec{r}$. It may be shown (see Appendix, Part C) that, for small deformations and at fixed $\vec{r}$, the correlation functions should be proportional to γ^2, where γ is the amplitude of the deformation. In the shear deformations performed here, there is no symmetry argument to obtain isotropic correlation functions, i.e., depending only on the modulus r of the interparticle vector $\vec{r}$. However, deviations from isotropic averaging are difficult to observe in practice and the correlation functions presented here are obtained by performing isotropic averaging on r.

Because we are interested in the reversibility of the macroscopic and microscopic states of the system in a large amplitude shear cycle, we compute here the nonaffine displacements after a cycle in which the system has relaxed to zero stress for a long time after shearing to a large amplitude (this is state (II) in Figure 4). The results are plotted in Figure 6. It is observed that $g_{yy}(r)$ and $g_{xx}(r)$ are nearly identical. This could be expected because, in the limit of small deformations, the deformation fields along both x and y directions are equivalent within a rigid rotation, which leaves the correlation functions unchanged. This large deformation behavior is thus reminiscent of the small

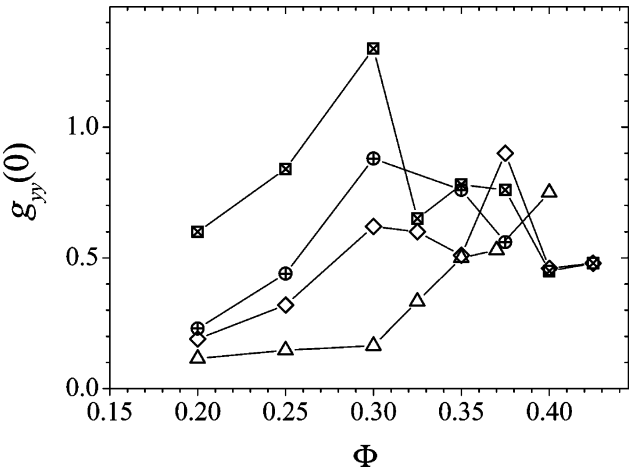

Figure 7. Amplitude $g_{yy}(0)$ of the correlation function of nonaffine displacements after a shear cycle of amplitude $\gamma_{max} = 2.0$, as a function of the volume fraction Φ for different value of the connectivity n: (crossed square) $n = 8.5$, (⊕) $n = 9$, (◇) $n = 10$; (△) $n = 12$.

deformation behavior. On the other hand, although still comparable, $g_{zz}(r)$ is significantly smaller than $g_{yy}(r)$ and $g_{xx}(r)$. Then, although much smaller than the other components, $g_{xy}(r)$ is nonzero. This is a finite size effect because this function should be identically zero in a macroscopic system for symmetry reasons. The amplitude measured for $g_{xy}(r)$ is of order 0.1, which illustrates the $N^{-1/3}$ scaling of the fluctuations for the stress values discussed above (see Appendix, Part B).

The value of $g_{yy}(0)$ is plotted in Figure 7 as a function of the volume fraction of hard inclusions Φ, for various values of the connectivity n, for a macroscopic deformation of amplitude $\gamma_{max} = 2.0$. $g_{yy}(0)$, tends to increase up to $\Phi \approx 0.3$ and then stabilize or decrease. Another feature is that this quantity is a decreasing function of the parameter n: it is smaller for more strongly connected systems, i.e., for less-disordered systems. Specifically, a strongly connected system ($n = 12$) displays a much smaller nonaffine amplitude, especially for volume fractions Φ smaller than 0.3−0.35. A qualitative picture of the particle displacements may be drawn as follows. A loosely connected network favors a disordered, i.e., nonaffine response of the system, and thus a large value of $g(0)$. The role of the filler particle is less straightforward. On one hand, the filler-excluded volume creates free energy barriers that might tend to favor affinity by a caging-like effect (mechanism (I)). On the other hand, once a free energy barrier has been crossed under the action of the imposed deformation, it may be very difficult for the system to drop back in its initial relative position (mechanism (II)). This second mechanism tends to favor the nonaffine nature of the microscopic displacements. The behavior observed in Figure 7 results from these two competing mechanisms. From the results in Figure 7, we deduce that mechanism (II) is dominant at low filler volume fraction in the case of disordered (i.e., loosely connected) systems, whereas mechanism (I) dominates at a larger filler volume fraction. Specifically, this is the case for the $n = 8.5$ samples. On the other hand, for a much more strongly connected system ($n = 12$), mechanism (II) becomes more dominant on increasing the filler volume fraction, at least up to $\Phi = 0.42$. Note that the value above which the fillers favor affinity may depend on the amplitude of the applied deformation.

4C. Elastic and Plastic Regimes. We consider here the ability of the system to recover its initial macroscopic shape after deformation. Because the phase space of the relevant degrees of freedom is very complex, with large free energy barriers, there is indeed no reason the system should actually recover its initial microscopic and macroscopic states. The possible residual strain at long times after an applied stress has been removed corresponds to plastic deformation. On the other hand, we expect that, for small deformations, the initial state of the system, both macroscopically and microscopically, is recovered once the external constraint is suppressed. This corresponds to the elastic regime. We aim at characterizing both the elastic and plastic regimes here. For this purpose, shear cycles are applied according to the procedure described above (Section 3D). The systems are first sheared at constant $\dot{\gamma}$ ($\dot{\gamma} = 0.1$ typically) up to various maximum shear γ_{max} and then relaxed to zero shear stress according to the iterative procedure described in Section 3D. During the relaxation process, the applied deformation tensor is of the form (see eq 12)

$$\frac{(I_d + d\Gamma)}{[\det(I_d + d\Gamma)]^{1/3}} = \begin{bmatrix} \gamma_1 & d\gamma_1 & \epsilon \\ d\gamma_1 & \gamma_2 & \epsilon \\ \epsilon & \epsilon & \gamma_3 \end{bmatrix} \tag{17}$$

with $d\gamma_1 = -C\sigma_{xy}$. The quantities ϵ are proportional to $N^{-1/3}d\gamma_1$ and are much smaller than the other tensor elements. The fact that these elements are not zero is a finite size effect, directly related to the fact that correlation functions such as g_{xz} do not cancel by symmetry as they would in a macroscopic system. The diagonal elements λ_i differ from 1 by a quantity of order ϵ as well. To preserve the pure shear symmetry of the deformation tensor Γ (cf. eq 14), a subsequent infinitesimal rotation must be applied at each time step, because the stress tensor is symmetric by construction: $\sigma_{xy} = \sigma_{yx}$. This rotation is defined by the tensor

$$\mathbf{R} = \begin{bmatrix} \cos\theta & \sin\theta & 0 \\ -\sin\theta & \cos\theta & 0 \\ 0 & 0 & 1 \end{bmatrix} \tag{18}$$

with $\cos\theta = \lambda_1/\sqrt{\lambda_1^2 + d\gamma_1^2}$ and $\sin\theta = d\gamma_1/\sqrt{\sqrt{\lambda_1^2 + d\gamma_1^2}}$, so that the resulting deformation tensor Γ retains at any time the symmetry of a simple shear (eq 14) within small tensor elements of order $N^{-1/3}\gamma$, where γ is the shear amplitude:

$$\Gamma = \begin{bmatrix} \lambda_1 & \gamma & \epsilon \\ 0 & \lambda_2 & \epsilon \\ \epsilon & \epsilon & \lambda_3 \end{bmatrix} \tag{19}$$

Two criteria have to be satisfied at the end of the way back to equilibrium: the stress tensor must be isotropic, and the total duration must be longer than the relaxation time of the system. The nonisotropic stress elements are canceled with a precision better than 10^{-4}, and the total duration of equilibration consists of at least 1000 deformations of duration 30 time steps $dt = 0.02$ s, that is, at least 600 elementary time units (sec). This is significantly longer than the relaxation time of the stress, which is typically a few tens of sec in these systems.[50]

We first consider the case of small deformations. After applying deformations of amplitude smaller or equal to 0.15, we allow the anisotropic part of the stress to relax to zero (according to the procedure described above). During the stress relaxation process, the relaxations of all elements of the deformation tensor Γ (actually the elements of the tensor $\Gamma - I_d$) are monitored as a function of time. An example of such relaxations is given in Figure 8 for $\gamma_{max} = 0.15$. At $t = 0$, all tensor elements are zero except γ_{xy}, because Γ then corresponds to the imposed shear deformation given by eq 14. During relaxation, γ_{xy} relaxes toward a small value of order 10^{-3},

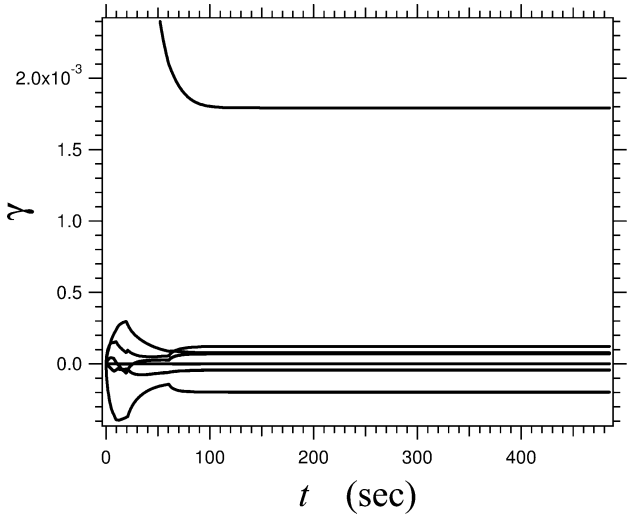

Figure 8. Relaxation of the tensor element γ_{xy}, as well as the other elements of the deformation tensor as a function of time (same system as in figure 9). All these elements relax to zero, within 10^{-3} as far as γ_{xy} is concerned, and less than a few 10^{-4} for the other tensorial elements. This corresponds to the elastic regime.

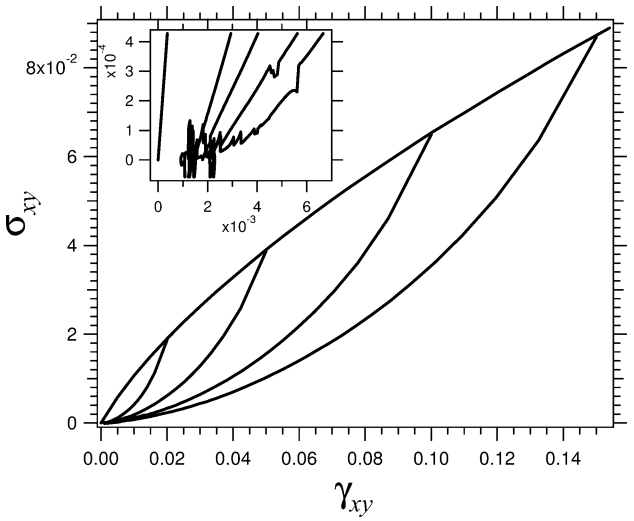

Figure 9. Shear cycles of varying, small amplitudes: the system is sheared at $\dot{\gamma} = 0.1$ up to γ_{max} and then the anisotropic stress relaxes to zero for at least 600 s. For deformations of amplitude smaller than 0.15 as shown here, the system ($\Phi = 0.35$, $n = 8.5$) relaxes toward its initial shape in a finite time.

whereas all other elements relax to a final value of order 10^{-4} after first increasing somehow. The relaxation of the shear stress may also be monitored as a function of γ_{xy}. Strain−stress shear cycles are plotted in Figure 9 for various maximum amplitudes smaller than 0.15. Within the interval $0.025 < \gamma_{max} < 0.15$, the final value of γ_{xy} does *not* depend on the amplitude of deformation γ_{max}. This nonzero, albeit very small, value is probably due to some instabilities within the sample that have not been entirely removed by the second preparation step. On the other hand, once this instability has been suppressed by the shear deformation, the system retains a reference state that does not depend on the applied deformation, up to γ_{max} of the order 15%. In any case, the final values of the deformation tensor are more than 2 orders of magnitude smaller than the initial deformation so that we can consider that the sample recovers its initial shape. This corresponds to the elastic regime.

Stress/strain shear cycles of large amplitude are plotted in Figure 10 for various maximum deformations γ_{max}. The zoom in the inset in Figure 10 clearly shows that some residual shear

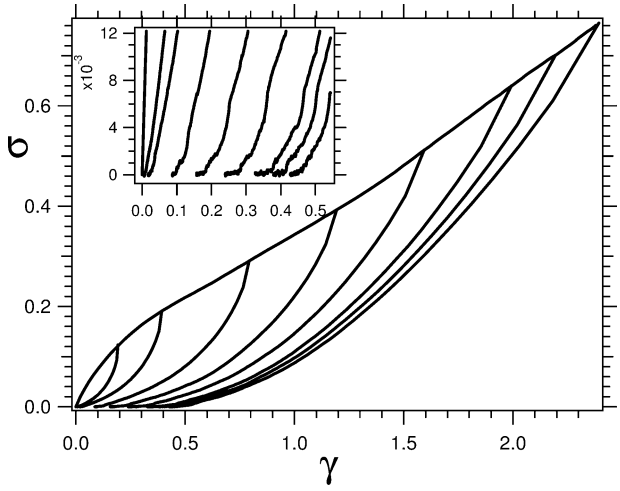

Figure 10. Stress−strain cycle in the system $n = 8.5$, $\Phi = 0.35$. The system is sheared at a shear rate $\dot{\gamma} = 0.1$ to various values of the maximum stress γ_{max} and then relaxed to zero stress in the iterative, quasistatic procedure described in the text. Inset: zoom of the return curves at low stress values to show the residual strain.

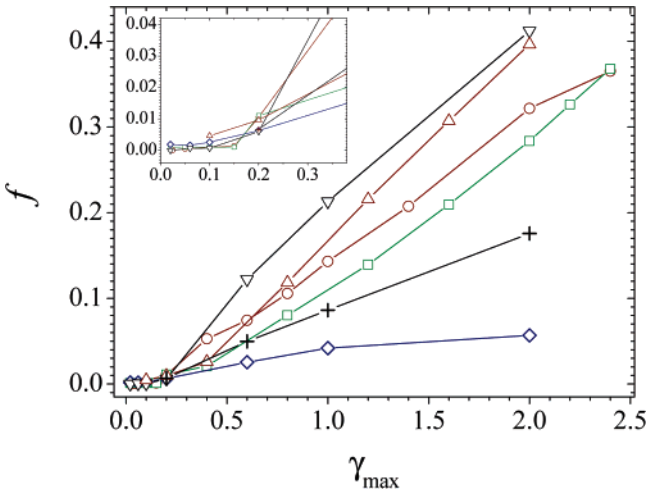

Figure 11. Residual deformation f (plasticity) at the end of the way back to equilibrium as a function of the maximum strain γ_{max} in various systems: (◇) $\Phi = 0.20$, $n = 12$; (+) $\Phi = 0.325$, $n = 12$; (▽) $\Phi = 0.40$, $n = 12$; (□) $\Phi = 0.35$, $n = 8.5$; (○) $\Phi = 0.375$, $n = 10$; (△) $\Phi = 0.375$, $n = 9$. The inset is a zoom of the curves at small deformations to emphasize the onset of the plastic regime.

deformation f (plasticity) remains after relaxation and that it depends in a sensitive way on the amplitude γ_{max}. This corresponds to the plastic regime. As mentioned above, the system is allowed to relax for several hundreds of seconds, and it is indeed observed that the shear stress cancels (to a precision of the order 10^{-4}), while the residual deformation remains roughly constant, after a few hundred seconds. This means that the system has reached a macroscopic (mechanical) steady state, which however does not necessarily correspond to a true thermodynamic equilibrium.

The residual strain f (plasticity) is plotted as a function of the maximum strain γ_{max} in Figure 11 for systems with various volume fractions Φ and connectivities n. The inset in Figure 11 shows that the variation of f as a function of γ_{max} is not linear. Specifically, there is no measurable residual deformation for maximum strain values γ_{max} smaller than 0.15. The onset of plasticity seems to vary from, roughly, 0.10 to 0.20 according to the system. Note that this is significantly *larger* than the onset of the nonlinear regime in the mechanical response, which is estimated to be of the order 0.03, as mentioned in Section 4A.

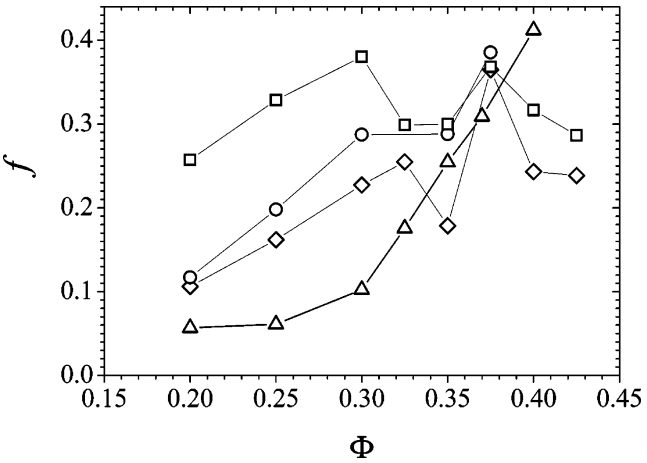

Figure 12. Residual deformation f as a function of the volume fraction Φ for different values of the connectivity n: (□) $n = 8.5$; (○) $n = 9$; (◇) $n = 10$; (△) $n = 12$. All points are obtained with a value $\gamma_{max} = 2.0$.

Beyond the onset of plasticity, the residual deformation increases roughly linearly with the amplitude of deformation γ_{max}. In the range of n and Φ investigated here, all systems exhibit qualitatively the same relationship between γ_{max} and the residual deformation f. Several features may be emphasized. In strongly connected systems (i.e., for $n = 12$), the plastic deformation f increases as Φ increases: for a deformation amplitude $\gamma_{max} = 2.0$, it varies from 0.05 (at $\Phi = 0.20$) to 0.4 (at $\Phi = 0.40$). The residual strain f (plasticity) is plotted as a function of the volume fraction Φ in Figure 12 for different values of the connectivity n and for an amplitude $\gamma_{max} = 2.0$. The results in Figure 12 show in particular that a strong network, i.e., a high value of the connectivity n, tends to reduce the plasticity of the system. On the other hand, the presence of the fillers tends to favor the plastic behavior, at least for the large shear deformations considered here. The case of the systems with $n = 12$ is particularly striking. At filler volume fractions smaller than 0.30, the plastic deformation is much smaller than in the more disordered, or loosely connected systems. However, at larger filler volume fraction, the plasticity is comparable to that measured in other systems. This result has to be compared with that in Figure 7 regarding the dependence on Φ of the nonaffinity $g_{yy}(0)$. Both quantities show a qualitatively similar behavior.

4D. Local Reorganizations and Bucklings. In this section, we shall characterize local reorganizations in a way complementary to nonaffine displacements studied in Section 4B by defining local topological changes that we call bucklings, as illustrated in Figure 13a. Bucklings are defined in the following way. In the reference state (I), consider a site i at position $\vec{R}_i$ and the ensemble of all its neighbors, connected by an elastic spring to i. For three sites j, k, l ($j \neq l \neq k$), which belong to the ensemble of neighbors to i, a tetrahedron is defined by the set of three vectors $\vec{R}_{ij} = \vec{R}_j - \vec{R}_i$, $\vec{R}_{ik} = \vec{R}_k - \vec{R}_i$, $\vec{R}_{il} = \vec{R}_l - \vec{R}_i$ (see Figure 13a). The determinant $\Delta^{(I)}$ of the matrix constructed with the three vectors gives the volume of the tetrahedron. Sites j, k, l may always be ordered such that $\Delta^{(I)}$ is positive. In a subsequent state (II), the determinant $\Delta^{(II)}$ may become negative as site i has crossed the plane containing the sites j, k, l, as schematized in Figure 13a. Site i has thus jumped to a new position with a different local environment. We call buckling such a local topological inversion. To compare the determinant values in various states described by different deformation tensors, the determinants are computed using the particle positions $\vec{R}_{i(0)}$ taken in the reference state (see Figure 4), which

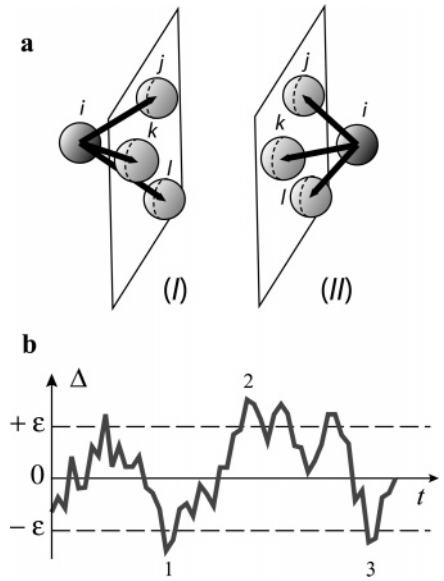

Figure 13. (a) Schematics illustrating a local buckling of site i. In state (I), the determinant constructed on the three vectors $\vec{R}_{ij}$, $\vec{R}_{ik}$, $\vec{R}_{il}$ is positive. It becomes negative in state (II) as site i falls in a new position of local equilibrium, crossing the plane containing the sites j, k, l. (b) Dynamics of buckling of a given tetrahedron. As indicated, one inversion is counted each time the value of the determinant has crossed the gap interval $[-\epsilon, +\epsilon]$.

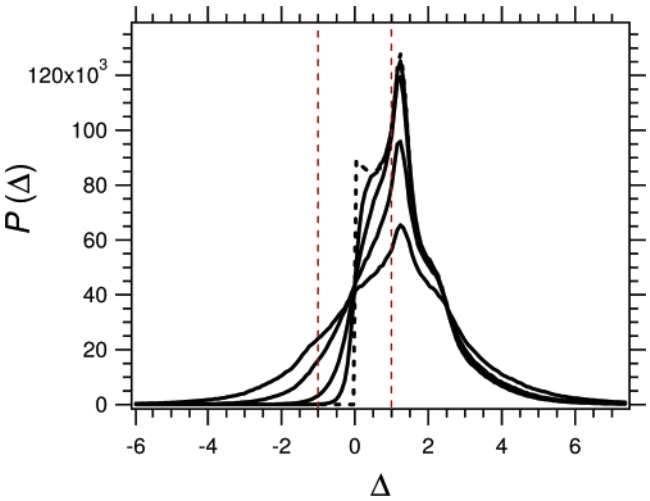

Figure 14. Histograms of the values Δ of the determinants, as defined in the text, in the system $n = 12$, $\Phi = 0.40$ sheared at $\dot{\gamma} = 0.1$, at increasing shear deformation (full curves: $\gamma = 0.2$, 0.4, 1.0, and 2.0). In the initial, undeformed state taken as reference (dotted curve), all determinants are chosen to be positive. Bucklings thus correspond to jumping from the region on the right-hand side of the threshold ϵ ($\epsilon = 1.0$ on the graph) toward the region on the left $\Delta < -\epsilon$.

is described by a unity deformation tensor. Actual bucklings correspond to jumping to a new position separated from the initial one by some energy barrier. We thus consider bucklings as jumps from a *finite*, positive threshold value $+\epsilon$, to a finite, negative value $-\epsilon$. Histograms of the determinant values during a large amplitude shear deformation of a system are shown in Figure 14. In the initial, undeformed state, which is taken as reference, all determinants are chosen to be positive. In the subsequent, deformed states, a fraction of the determinants become negative, which indicates the presence of local rearrangements. As seen from the histograms shown in Figure 14, the value of this threshold ϵ may be chosen of the order 0.2−1.0 typically.

Considering the process of buckling, the two different relaxation mechanisms (I) and (II) related to the presence of

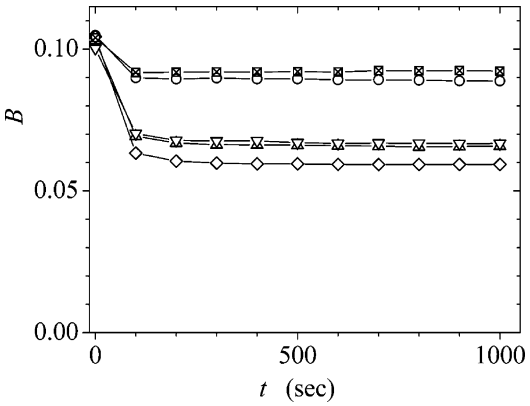

Figure 15. The fraction of bucklings B (defined as the ratio of the number of bucklings to the total number of tetrahedra) as a function of time during the way back to zero stress in a large amplitude shear cycle. The fraction of bucklings is computed here with respect to the initial, undeformed reference state. $\gamma_{max} = 2.0$. Threshold $\epsilon = 0.75$. Connectivity $n = 12$. (◇) $\Phi = 0.20$; (△) $\Phi = 0.25$; (▽) $\Phi = 0.30$; (○) $\Phi = 0.35$; (crossed square) $\Phi = 0.40$.

filler particles may be defined more precisely: (1) Mechanism (I). At large volume fraction, the steric hindrance due to fillers tends to impede bucklings: fillers create energy barriers that become more difficult to cross as the filler volume fraction increases. We expect this mechanism to contribute to the reduction of buckling, e.g., during an applied deformation. (2) Mechanism (II). The same steric hindrance makes it difficult for the system to relax back in its initial microscopic state as the system relaxes back to zero deviatoric stress at the end of a deformation cycle. Thus, we expect the presence of the fillers to have contradictory effects, one which favors affine, reversible deformations and the other one which favors nonaffine and irreversibility. The irreversible nature of the microscopic evolution of the system will thus depends on which of these processes dominates.

1. Bucklings during Relaxation to Zero Stress in a Shear Cycle. In Figure 15, the fraction of bucklings B (defined as the ratio of the number of bucklings to the total number of tetrahedra) is plotted as a function of time during the relaxation to zero deviatoric stress in systems sheared up to $\gamma_{max} = 2.0$ for different values of the filler volume fraction Φ and a high connectivity ($n = 12$). The fraction of bucklings is referred here to the initial, undeformed reference state. In all the systems considered here, this fraction is close to 0.1 at deformation $\gamma_{max} = 2.0$ prior to stress relaxation ($t = 0$), which means that the effect of Φ on mechanism (I) is small. When the system relaxes to zero stress, the fraction of bucklings decreases in all systems, with an amplitude that decreases as Φ increases. This result indicates that the role of mechanism (II) increases as Φ increases, at least for the volume fractions and connectivity considered here. This result has to be compared with the fact that plasticity is larger as Φ is large in systems with $n = 12$ (see Figure 12): a large filler volume fraction prevents the system to relax back in its initial state. Note the sharp difference in behavior between $\Phi = 0.30$ and $\Phi = 0.35$, whereas below and above these values, respectively, the systems behave quite similarly.

The fraction of bucklings B at the end of a shear cycle, referred to the initial, undeformed state, is plotted as a function of the maximum amplitude γ_{max} in Figure 16 for various filler volume fractions Φ and connectivity $n = 12$. These results show that the buckling fraction B displays a threshold, in a way quite similar to plasticity (see Figure 11). This threshold has a similar value of about $\gamma \approx 0.15$. Here also, the buckling fraction

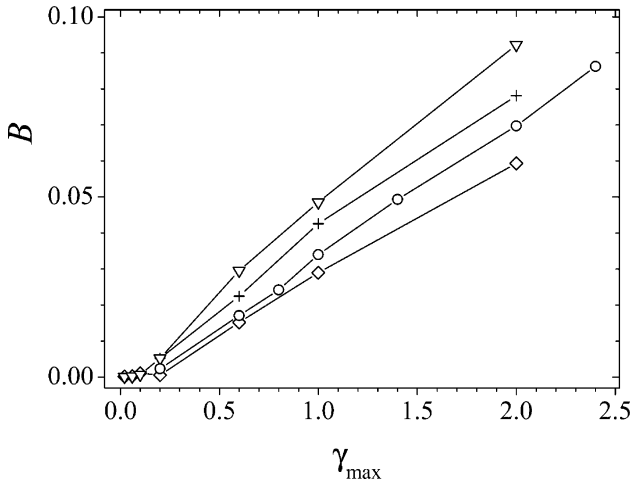

Figure 16. Fraction of bucklings B at the end of a shear cycle (i.e., after relaxation to zero deviatoric stress), referred to the initial, undeformed state, as a function of the maximum amplitude γ_{max}: (◇) $\Phi = 0.20$, $n = 12$; (+) $\Phi = 0.325$, $n = 12$; (▽) $\Phi = 0.40$, $n = 12$; (○) $\Phi = 0.37$, $n = 10$. Threshold $\epsilon = 0.75$.

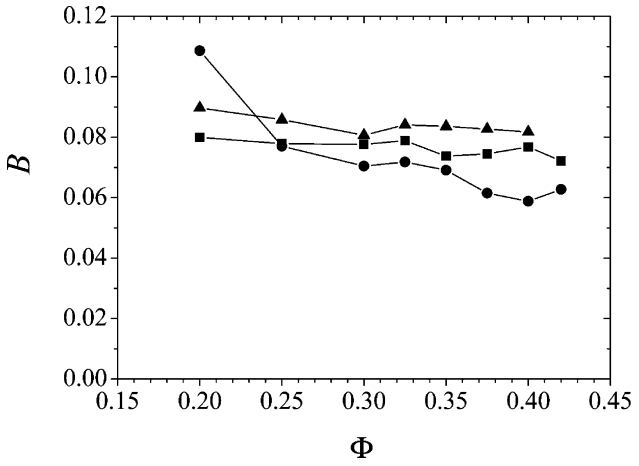

Figure 17. Fraction of bucklings B (referred to the initial equilibrium state) at the top of a large amplitude shear cycle, at amplitude $\gamma_{max} = 2.0$, as a function of the volume fraction Φ for different values of the connectivity n: (●) $n = 8.5$; (■) $n = 10$; (▲) $n = 12$ (same experiments as in Figure 18). The threshold value is $\epsilon = 0.75$.

increases as Φ increases, which means that mechanism (II) (returning to the initial state becomes more difficult) dominates over mechanism (I) (buckling under deformation becomes more difficult) as Φ increases.

In Figure 17, the fraction of bucklings at the top of a shear cycle of amplitude $\gamma_{max} = 2.0$, referred to the initial, undeformed state, is plotted as a function of the filler volume fraction, for three different values of the connectivity n: $n = 8.5$, $n = 10$, and $n = 12$. All curves are decreasing functions of Φ, although slightly in the more connected systems. This shows that, during deformation, the presence of filler particles impedes the buckling of tetrahedra. In Figure 18, the fraction of bucklings is plotted at the end of the same shear cycles as in Figure 17 after the same systems have relaxed back down to zero deviatoric stress. Increasing the filler volume fraction results in a slight increase of the buckling fraction B for the two larger values of the connectivity, and in a decrease of the buckling fraction in the more loosely connected, i.e., a more elastically disordered system.

The behaviors observed in Figures 17 and 18 illustrate the complex relaxation mechanisms in such systems. The buckling behavior results from several mechanisms. First, elastic disorder

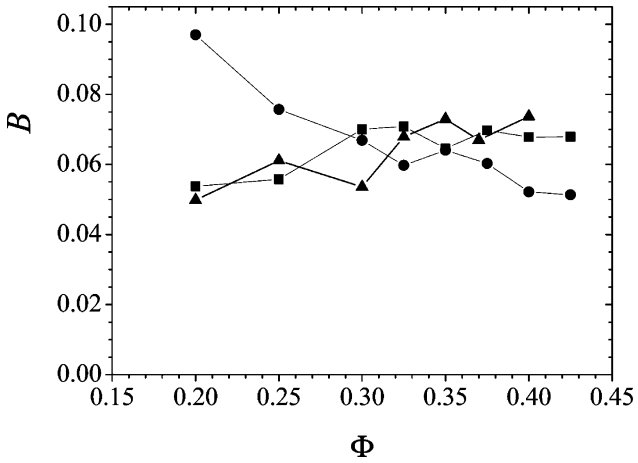

Figure 18. Fraction of bucklings B at the end of a large amplitude shear cycle, as a function of the volume fraction Φ for different values of the connectivity n: (●) $n = 8.5$; (■) $n = 10$; (▲) $n = 12$. The amplitude of the cycle is $\gamma_{max} = 2.0$; the threshold value is $\epsilon = 0.75$.

is a driving force for buckling. It is especially clear in Figure 17 when considering the case of $n = 8.5$ systems at low filler volume fraction. Indeed, a disordered or loosely connected elastic network favors complex reorganization when the system tries to minimize its free energy. On the other hand, one sees in both Figures 17 and 18 that the buckling fraction of loosely connected systems can decrease when increasing the filler volume fraction and becomes even smaller than that of more strongly connected systems. Thus buckling is the result of contradictory effects: the driving force due to the elastic disorder of the system and the barriers associated with mechanisms (I) and (II). Neither of these mechanisms can be considered separately, and the overall behavior is the result of their complex interaction.

2. Buckling Dynamics. In this section, we study the dynamics of the local inversions during the simulations. To get a statistical ensemble, one tetrahedron is chosen at random among the ensemble of tetrahedra attached to each site. The value of each tetrahedron is followed as a function of time during a given experiment, as schematized in Figure 13b. One inversion is counted each time the determinant value crosses the gap $[-\epsilon, +\epsilon]$. At each time step, the number of inversions performed from the beginning of the simulation and the time elapsed since the last inversion are stored for each tetrahedron. To illustrate the buckling dynamics in the system, the following experiment has been performed. The system is submitted to an oscillatory shear of the form $\gamma_{xy} = \gamma_{max} \sin \omega t$ with a period $T = 51.2$ s (pulsation $\omega = 2\pi/T = 0.1227$) and peak-to-peak amplitudes γ_{max} varying from $\gamma_{max} = 0.04$ to $\gamma_{max} = 1.63$. Ten cycles are performed. The number of inversions that occurred from the starting point is stored every quarter period for each tetrahedron in the representative set. Histograms of the buckling number during shear oscillations are plotted at different times t in Figure 19. The maxima of the oscillations in the curves at times t equal to an integer number of periods correspond to *even* numbers of bucklings. After an integer number of periods, the deformation tensor is I_d and more tetrahedra drop back in their initial configuration, which corresponds to an even number of jumps. The amplitude at $N = 0$ gives the number of tetrahedra that have *not* moved since $t = 0$. The fraction of bucklings referred to the initial, undeformed system is plotted in Figure 20 for various amplitudes γ_{max} between 0.04 and 1.63. The number of tetrahedra that have not moved since $t = 0$ is plotted in Figure 21. The curve does not seem to tend to a finite value at long times. Both Figures 20 and 21 illustrate that buckling is

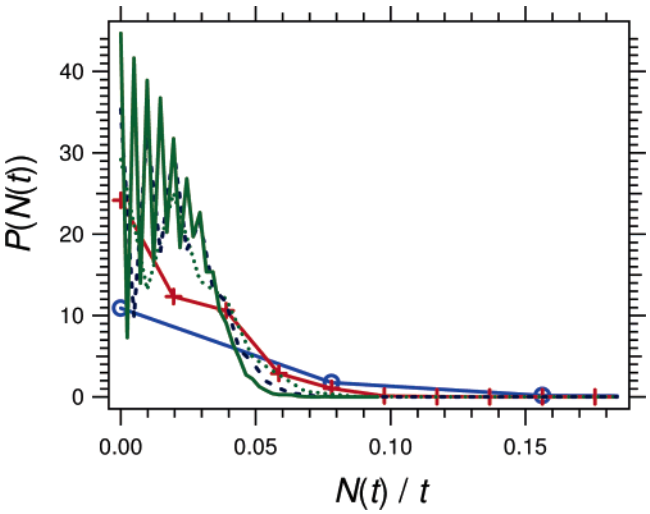

Figure 19. Probability densities $P(n(t)/t)$ of the number n of bucklings at time t in a representative ensemble of 10 000 tetrahedra during large amplitude shear oscillations (amplitude $\gamma_{max} = 1.63$, period $T = 51.2$ s), at different times t: (○) $t = 12.8$ s; (+) $t = 51.2$ s; dotted curve: $t = 102.4$ s; dashed curve: $t = 204.8$ s; full curve: $t = 409.8$ s. The amplitude at $n/t = 0$ on each curve (divided by t) gives exactly the fraction of tetrahedra which have not moved at the corresponding time t. Threshold $\epsilon = 0.75$. The oscillation maxima correspond to *even* numbers of bucklings (the distributions of buckling numbers are considered after an integer number of periods). The data are from a system with $n = 12$ and $\Phi = 0.40$.

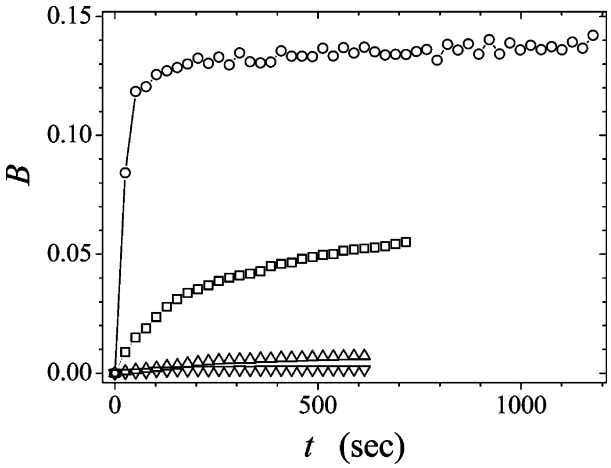

Figure 20. Fraction of bucklings B as a function of time during oscillatory cycles ($\gamma_{max} = 1.63$, period $T = 51.2$ s), in the system $\Phi = 0.40$, $n = 12$, for various amplitudes: (○) $\gamma_{max} = 1.63$; (□) $\gamma_{max} = 0.28$; (△) $\gamma_{max} = 0.08$; (▽) $\gamma_{max} = 0.04$. Threshold $\epsilon = 0.75$. B is plotted every half period, each time the system comes back to undeformed state.

negligible at small deformation amplitudes: this corresponds to the elastic regime.

It is interesting to estimate the relative number of tetrahedra that remain trapped in a buckled configuration with respect to the initial state at some point of their dynamics. To clarify this point, a two-time analysis may be performed as follows. At time t_1, the subensemble of tetrahedra which have been inverted, i.e., which have done an *odd* number of bucklings, are selected. The evolution of this subensemble is then followed as a function of subsequent time and may eventually be compared to the evolution of the full ensemble of tetrahedra. This is illustrated in Figure 21. It appears that the subensembles that have buckled at time $t_1 = 204.8$ s continue to undergo *more* inversions than the whole ensemble of tetrahedra on average. This behavior is even more pronounced at a smaller amplitude ($\gamma_{max} = 0.28$). The subensemble of tetrahedra inverted at time $t_1 = 204.8$

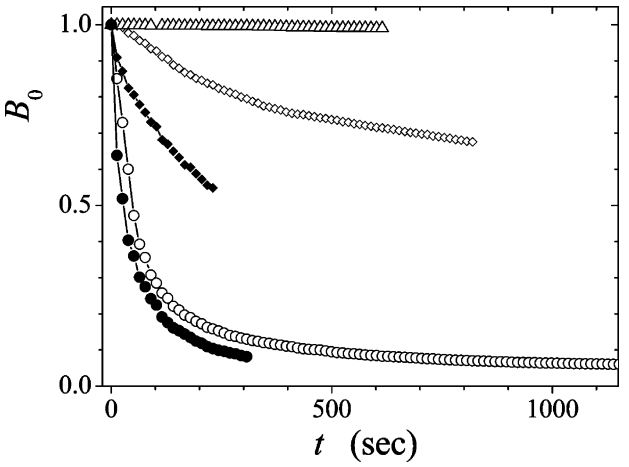

Figure 21. Fraction B of tetrahedra that have *never* buckled, as a function of time, during large amplitude oscillatory cycles (period $T = 51.2$ s), in the system $\Phi = 0.40$, $n = 12$, for various peak to peak amplitude of the oscillations: (○) $\gamma_{max} = 1.63$; (◇) $\gamma_{max} = 0.28$; (△) $\gamma_{max} = 0.08$. Threshold $\epsilon = 0.75$. This quantity is deduced from the amplitude at $N = 0$ of histograms such as those in Figure 19. In black, we display a two-time analysis of the buckling dynamics: the fraction of tetrahedra inverted at $t_1 = 104.8$ s have been selected. The curves give the fraction of this subensemble which have not subsequently buckled.

continue to move significantly more than the full tetrahedra ensemble. That means that part of the buckling takes place for the more mobile tetrahedra. On the other hand, for large deformations, Figure 21 shows also that all tetrahedra buckle at some point because there is no indication that the curves would relax to *finite* plateau values.

3. Irreversibility of Microscopic Deformations Due to Buckling. After applying a large amplitude strain cycle, the system exhibits a residual deformation, which depends on the amplitude γ_{max} of the strain. One question is to know whether this macroscopic residual deformation may be canceled by shearing again the system in the opposite direction with an appropriate amplitude. This procedure is illustrated in Figure 22. The system $n = 8.5$, $\Phi = 0.35$ has first been sheared at $\dot{\gamma} = 0.1$ up to $\gamma_{max} = 2.0$, then relaxed to zero deviatoric stress. From the obtained equilibrium state, which exhibits a residual shear deformation f, the system is then sheared at the opposite shear rate $\dot{\gamma} = -0.1$ "down" to different values γ^R_{max}, and then relaxed again to zero deviatoric stress. Two curves corresponding to $\gamma^R_{max} = -1.40$ and $\gamma^R_{max} = -1.80$ are shown in Figure 22. This illustrates that the macroscopic deformation may be canceled by applying a second opposite cycle at an amplitude comparable to that of the first cycle. However, the question to know whether the system has dropped into the same microscopic state as the initial state remains open at this point.

Because of the complexity of the phase space, the system does not necessarily reach a uniquely defined minimum energy state in a finite time. To illustrate this effect of the disorder, the average energy in the system has been computed throughout the simulations. The contributions from the elastic springs and the hard-core potentials may be treated separately. The average elastic energy per spring is defined as:

$$\langle E_{el} \rangle = \frac{1}{N_s} \sum_j E^j_{el} \tag{20}$$

where N_s is the number of springs and the sum runs over the ensemble of springs within the simulation box. The average excluded volume energy per particle pair is defined as:

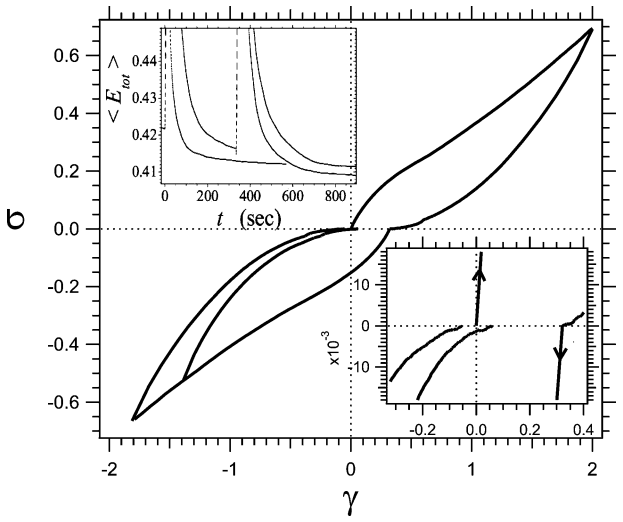

Figure 22. Cycle of large amplitude shear, followed by a second cycle in the opposite direction, in a system $n = 8.5$, $\Phi = 0.35$. The bottom right inset is a zoom of the stress−strain curves, which shows that the macroscopic plasticity may be canceled in this way. The arrows indicate the shear parts at constant $\dot{\gamma} = \pm 0.1$. Up left inset: the average total energy (defined in eq 22) as a function of time during the cycles. Time $t = 0$ is the starting point of the first cycle ($\dot{\gamma} = 0.1$), the two curves relaxing between $t \approx 0$ and $t \approx 300$ s corresponding to relaxation from $\gamma_{max} = 2.0$ (top curve) and $\gamma_{max} = 0.80$ (bottom curve), respectively. The second cycle ($\dot{\gamma} = -0.1$) starts at $t \approx 335$.

$$\langle E_{hs} \rangle = \frac{1}{N_{pair}} \sum_m E^m_{hs} \tag{21}$$

where the sum runs over the ensemble of interacting pairs. The total energy per particle (including both contributions) has also been computed as:

$$\langle E_{tot} \rangle = \frac{1}{N} \left(\sum_{spring} E^j_{el} + \sum_{pair} E^m_{hs} \right) \tag{22}$$

Note that, with the given definitions, $\langle E_{tot} \rangle \neq \langle E_{el} \rangle + \langle E_{hs} \rangle$. The evolution of the energy throughout large-amplitude stress−strain cycles is plotted as an inset in Figure 22. Several observations may be drawn from this graph. First, the energy state in which the system drops after relaxation is not unique. It depends on the mechanical history of the system, namely here on the maximum shear γ_{max}. Second, the system drops in a state of *lower* energy after shearing at large amplitude. The tendency to decrease the energy is observed for both individual contributions (average elastic energy and average excluded volume energy). Note that this drop in energy is possible because our sample is relatively "young". But we emphasize that, even after the third preparation step, the internal energy of the sample can decrease as a consequence of the very complicated phase space available to the filler particles.

To illustrate further the hysteretic behavior of such systems at large imposed deformations, we consider the variance $\langle \Delta R^2 \rangle$, which characterizes the nonaffinity of the microscopic displacements at the scale of the filler particles. This quantity is obtained by taking the second moment of the histograms $P(\Delta R)$ for the modulus of the nonaffine displacement vectors $\Delta R^2 = (\Delta X^2 + \Delta Y^2 + \Delta Z^2)$, as defined in Section 4B. The quantity $\langle \Delta R^2 \rangle^{1/2}$ measured at the end of shear cycles is plotted as a function of the residual strain f (plasticity) in Figure 23 for various systems, and various maximum deformation amplitudes, corresponding thereby to various values of the residual shear strain. Apart from a nonzero value of $\langle \Delta R^2 \rangle$ at zero value of the plasticity f, the

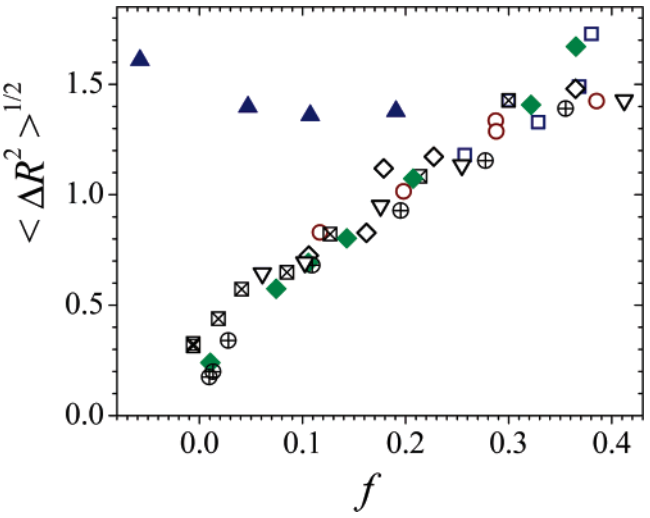

Figure 23. Average displacement $\langle \Delta R^2 \rangle^{1/2}$ (computed from the second moment of the histograms), as a function of the residual deformation f, for different values of the volume fraction Φ, connectivity n, and maximum strain γ_{max}: (□) $n = 8.5$, Φ varying from 0.20 to 0.375, $\gamma_{max} = 2.0$; (○) $n = 9$, Φ varying from 0.20 to 0.37, $\gamma_{max} = 2.0$; (◇) $n = 10$, Φ varying from 0.20 to 0.375, $\gamma_{max} \approx 1.9$; (crossed square) $n = 8.5$, $\Phi = 0.35$, γ_{max} varying from 0.1 to 2.0; (◇) $n = 10$, $\Phi = 0.375$, γ_{max} varying from 0.2 to 2.4; (⊕) $n = 9$, $\Phi = 0.375$, γ_{max} varying from 0.1 to 2.0; (▲) points obtained after a second cycle shearing at $\dot{\gamma} = -0.1$ down to different values γ_{max}^R (respectively −0.6, −1.0, −1.4, −1.8).

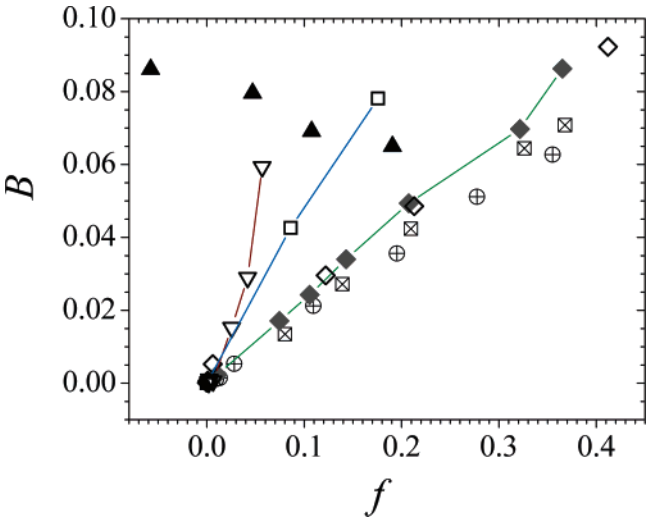

Figure 24. Fraction of bucklings B (defined as the total number of bucklings divided by the total number of tetrahedra) at the end of a shear cycle, as a function of the residual deformation f, for different values of the maximum strain γ_{max} in systems with various volume fraction Φ and connectivity n: (◇) $n = 12$, $\Phi = 0.40$, γ_{max} varying from 0.02 to 2.0; (crossed square) $n = 8.5$, $\Phi = 0.35$; (⊕) $n = 9$, $\Phi = 0.375$; (□) $n = 12$, $\Phi = 0.325$; (▽) $n = 12$, $\Phi = 0.20$, γ_{max} varying from 0.1 to 2.0; (♦) $n = 10$, $\Phi = 0.375$, γ_{max} varying from 0.2 to 2.4; (▲) points obtained after a second cycle shearing at $\dot{\gamma} = -0.1$ down to different values γ_{max}^R (respectively −0.6, −1.0, −1.4, −1.8), as illustrated in Figure 23.

variance $\langle \Delta R^2 \rangle$ varies linearly with the amplitude f. $\langle \Delta R^2 \rangle$ values obtained at the end of a second reverse cycle with various negative amplitudes (see Figure 22) are plotted also in Figure 23. Whereas the imposed reverse deformation tends to suppress the macroscopic residual deformation f, the nonaffine displacement $\langle \Delta R^2 \rangle$ remains unaffected; even though the macroscopic quantity f may be canceled by applying an appropriate counterdeformation, it is impossible to suppress the microscopic hysteresis of the displacement field.

To illustrate the relationship between plasticity and microscopic irreversibility, the fraction of bucklings B is plotted as a function of the plasticity f in Figure 24 for various systems and various maximum deformation amplitudes, corresponding thereby to various values of f. B is measured at the end of shear cycles, that is, the final state of each tetrahedron is considered (at the end of the way back to zero stress) and compared to the initial state. In the same way as in Figure 23, the fraction of bucklings B measured after second reverse cycles with various negative deformations, which suppress the macroscopic residual deformation (see Figure 22), is also plotted in 24. It is clear that plasticity correlates very well to the fraction of local topological changes (bucklings) during a large amplitude cycle. For a given system, a linear relationship between the residual deformation and the buckling fraction is approximately observed. Note that the slope of each of these curves depends strongly on the considered system. However, in a second reverse cycle, even though the macroscopic plasticity can be canceled by an appropriate deformation amplitude, the local configurations are not recovered. The number of topological inversions (as referred to the initial state) does not cancel and tends to increase even more. This illustrates the irreversible nature of the microscopic reorganizations under applied strain. The fraction of bucklings B at the end of shear cycles of fixed maximum amplitude $\gamma_{max} = 2.0$ is plotted as a function of the residual deformation f in Figure 25. Indeed, very different plastic behavior, that is, very different values of the plasticity f, are observed in various systems, specifically in systems with various connectivities,

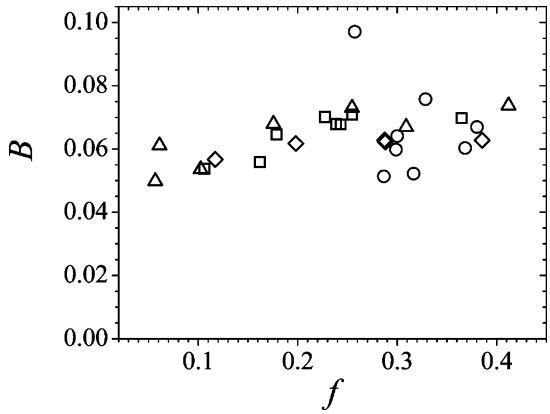

Figure 25. Fraction of bucklings B at the end of a shear cycle of fixed maximum amplitude $\gamma_{max} = 2.0$, as a function of the residual deformation f, for different values of the volume fraction Φ and connectivity n: (○) $n = 8.5$, $\Phi = 0.20-0.425$; (◇) $n = 9$, $\Phi = 0.20-0.425$; (□) $n = 10$, $\Phi = 0.20-0.425$; (△) $n = 12$, $\Phi = 0.20-0.40$.

whereas the fractions of bucklings observed in all these systems are comparable.

5. Conclusion

We have proposed a model in order to simulate on a mesoscopic scale the dynamical behavior of thermoplastic elastomers or reinforced rubbers in the high-temperature regime. This model represents a disordered elastic system made of hard spheres connected by harmonic springs. The parameters of the model are the connectivity n and the volume fraction Φ. Disorder is introduced by the dispersion of connectivity (see Figure 2). The connection between our mesoscopic model and a more precise description of thermoplastic elastomers is relatively direct: such systems are indeed rigid beads connected by polymer chains. In the case of filled elastomers, we expect our model to be more relevant in the case of weakly reticulated rubber matrixes, for which the elastic disorder is more important than in the case of strongly reticulated networks. In this latter

case, the model could be adapted by increasing the connectivity n and reducing its dispersion. In any case, subsequent work will be needed for establishing a quantitative mapping between real systems (thermoplastic or filled elastomers) and the present model, that is, relating the actual morphology of the systems to the parameters of the model. On the other hand, our model allows for the first qualitative analysis of mesoscopic relaxation of such systems and for analyzing their plastic behavior.

The response of the system to large-amplitude shear deformations has been studied by dissipative particle dynamics. The simulated systems exhibit some major effects that correspond to the behavior effectively observed in thermoplastic elastomers or filled rubbers. First, they allow reproduction of the reinforcement observed in the high-temperature regime in refs 65 and 66 as a function of the filler volume fraction. Second, our simulations display the nonaffinity of the microscopic displacements that have been observed in systems such as gels or rubbers. The plastic deformation of samples submitted to large-amplitude deformations may also be studied in our simulations. The systems exhibit an elastic regime in which they are able to recover their initial shape. This elastic regime corresponds here to deformations smaller than about 15%. At larger deformations, our simulations show that such systems exhibit a marked plastic behavior. Plasticity thresholds of real systems are not precisely documented in the literature. On the other hand, the amplitude of the plasticity observed in our simulations, between 0.05 and 0.20 for a deformation amplitude $\gamma_{max} = 1.0$, is typical of what is observed on thermoplastic elastomers[4,10−25] Note that chain pull out has often been proposed as a mechanism leading to plasticity. It is indeed very important to reduce this effect to control the mechanical behavior of thermoplastic elastomers. However, our simulations show that even if chain pull out can be reduced (e.g., by considering large molecular weight glassy blocks, or blocks with high T_g), controlling plasticity requires a very fine control and reduction of the elastic disorder of the samples. For real thermoplastic elastomers, that corresponds to a large number of connections between glassy beads (i.e., a large number of chains per bead, and as few loops as possible) and to a small dispersion in the quality of the connection between various beads. In the case of filled elastomers, that would correspond to a strongly reticulated matrix with strong anchorage to the filler and a good dispersion.

The simulations show that the plastic behavior of the system is strongly correlated to the tendency toward nonaffine deformations on a microscopic scale. On the other hand, even though the initial shape may be recovered by applying appropriate counterdeformations, the microscopic reorganization of the network is irreversible: the state of such systems thus depends on their history. Our simulations show that the elastic behavior is favored by a more strongly reticulated rubber matrix and that elastic disorder is a driving force for microscopic irreversibility. Indeed, the smaller the connectivity n, the larger the nonaffinity of the microscopic motion and the fraction of bucklings. The same simulations show that the presence of the fillers results in two competing effects. The first one, which we called mechanism (I), is a cage-like effect and contributes to reducing microscopic irreversibility. The second one, mechanism (II), tends to make the bucklings irreversible by preventing the system to relax back in its initial microscopic state. The microscopic and macroscopic behavior depends on which mechanisms dominate. We have shown that large filler volume fractions favor plastic behavior. On the other hand, large filler volume fractions might be useful to obtain systems with a high shear modulus. To better control the plastic behavior, our simulations suggest that a better way to achieve high shear modulus would be to consider systems made of shorter chains and smaller glassy bead volume fractions for instance. More generally, our model and simulations open the way for a large scope of investigations aimed at determining the phase space regarding elastic and plastic behavior to help designing systems with tailored properties. Our approach should be of interest for designing reinforced elastomers with improved elastic behavior. This kind of approach should be extended to describe in more detail the nonlinear behavior of gels and rubbers, and also the complex and fascinating behavior of filled elastomers in the low-temperature regime, in which glass transition effects lead to dramatic reinforcement and very strong nonlinear phenomena.[1,8,65−67]

Acknowledgment. Both authors are CNRS researchers.

Appendix

A. Torque. The torque acting on the system can be written as

$$\vec{T} = \sum_i \vec{R}^i \wedge \vec{F}^i \tag{23}$$

where the force $\vec{F}^i$ is the total force acting on particle i. The torque can be written as

$$\vec{T} = \sum_{i,j\text{neighbors}} \vec{R}^i \wedge \vec{F}^{i,j} \tag{24}$$

where the summation runs other all internal forces. $\vec{F}^{i,j}$ is the force that particle j exerts on particle i. The torque can then be written as

$$\vec{T} = \frac{1}{2} \sum_{i,\,j\text{neighbors}} (\vec{R}^i - \vec{R}^j) \wedge \vec{F}^{i,j} \tag{25}$$

Because all the forces between particles are central forces, this quantity is zero.

B. Deviation of the Initial Stress Tensor. In a macroscopic sample, the stress should be diagonal immediately after the particles have been randomly distributed in the sample because the sample would be isotropic. On the other hand, because of the finite number of particles in our sample, fluctuations cannot be neglected. After the particles have been distributed, the deviation of nondiagonal elements of the stress tensor can be estimated as:

$$\langle {\sigma_{\alpha\beta}}^2 \rangle = \frac{1}{V^2} \sum_{i,\,j} \langle R^i_\alpha R^j_\alpha F^i_\beta F^j_\beta \rangle \tag{26}$$

We consider the case of nondiagonal elements $\alpha \neq \beta$. Then, the previous sum, which contains N^2 terms a priori, effectively contains a number of order N of non-negligible terms only. Indeed

$$\langle R^i_\alpha R^j_\alpha F^i_\beta F^j_\beta \rangle \approx 0 \tag{27}$$

for indices corresponding to particles far apart. Thus

$$\langle {\sigma_{\alpha\beta}}^2 \rangle = \frac{1}{V^2} \sum_{i,j\text{neighbors}} \langle R^i_\alpha R^j_\alpha F^i_\beta F^j_\beta \rangle \approx \frac{1}{V^2} \sum_{i,j\text{neighbors}} \langle R^i_\alpha R^j_\alpha \rangle \langle F^i_\beta F^j_\beta \rangle \tag{28}$$

When the indices i and j are different, one has, if the particles i and j are neighbors

$$\langle F_\beta^i F_\beta^j \rangle = \langle (\sum_k \vec{F}^{i,k})(\sum_m \vec{F}^{j,m}) \rangle = \langle F^{i,j} \vec{F}^{j,i} \rangle \ (\approx -f^2) \quad (29)$$

where f is the typical force exerted by the elastic springs or by the hard core repulsion. If the particles are not neighbors, this average is zero. When the indices i and j are equals, one has

$$\langle F_\beta^i F_\beta^i \rangle = \langle \sum_j \vec{F}^{i,j} \vec{F}^{i,j} \rangle \quad (30)$$

These terms exactly cancel the previous ones, except for the bonds at the boundaries that point out of the box. The contribution of the remaining terms is therefore

$$\langle {\sigma_{\alpha\beta}}^2 \rangle \approx \frac{L^2}{V^2} \sum_{i,B} f_i^2 \approx \frac{L^2}{V^2} f^2 N_B \quad (31)$$

The subscript B means that the summation is performed over all particles that interact through the boundary of the box. The number of such particles is N_B. Finally:

$$\langle {\sigma_{\alpha\beta}}^2 \rangle \approx \frac{f^2 N_B L^2}{V^2} \propto N^{-2/3} \quad (32)$$

Thus, for a box with 10^4 particles, the amplitude of nondiagonal elements of the stress tensor is of the order 0.1 and is therefore not negligible.

C. Amplitude of the Correlation Functions. Let us consider an elastic body with a nonhomogeneous elastic modulus $\mu = \mu_0 + \delta\mu$. When this system is submitted to an imposed deformation γ, the displacement field $\vec{u}(\vec{r})$ is such that $\mu(\vec{r})\vec{u}(\vec{r}) \sim \gamma\mu_0$ is constant. It follows that $\delta u(\vec{r}) \sim \gamma \delta\mu(\vec{r})$, where $\delta u(\vec{r})$ is the local distortion as compared to the macroscopic affine deformation, i.e., the nonaffine displacement. Then:

$$\langle u(\vec{r}_i) u(\vec{r}_i + \vec{R}) \rangle \sim \gamma^2 \langle \delta\mu(\vec{r}_i) \delta\mu(\vec{r}_i + \vec{R}) \rangle \quad (33)$$

This shows that, for small deformations, the correlation function of the nonaffine displacements varies as a function of γ like γ^2.

References and Notes

(1) Nielsen, L. E.; Landel, R. F. *Mechanical Properties of Polymers and Composites*; Marcel Dekker: New York, 1994.
(2) Heinrich, G.; Klüppel, M. *Adv. Polym. Sci.* **2002**, *160*, 1−44.
(3) Medalia, A. I. *Rubber Chem. Technol.* **1986**, *60*, 45−61.
(4) Kazanci, M.; Cohn, D.; Marom, G.; Migliaresi, C.; Pegoretti, A. *Composites, Part A* **2002**, *33*, 453−458.
(5) Hur, S.; Hong, S. I.; Lee, H. J.; Han, S. W.; Kim, J. H.; Kang, J. Y.; Choi, B.-I.; Oh, C.-S. *Key Eng. Mater.* **2004**, *270*−*273*, 1107−1112.
(6) Payne, A. R. *J. Appl. Polym. Sci.* **1965**, *9*, 1073−1082.
(7) Harwood: J. A. C.; Mullins, L.; Payne, A. R. *J. Appl. Polym. Sci.* **1965**, *9*, 3011−3021.
(8) Kraus, G. *J. Appl. Polym. Sci., Appl. Polym. Symp.* **1984**, *39*, 75−92.
(9) Edwards, D. C. *J. Mater. Sci.* **1990**, *25*, 4175−4185.
(10) Mars, W. V.; Fatemi, A. *Int. J. Fatigue* **2002**, *24*, 949−961.
(11) Pego, A. P.; Grijpma, D. W.; Feijen, J. *Polymer* **2003**, *44*, 6495−6504.
(12) Schmalz, H.; Böker, A.; Lange, R.; Krausch, G.; Abetz, V. *Macromolecules* **2001**, *34*, 8720−8729.
(13) Schmalz, H.; Abetz, V.; Lange, R.; Soliman, M. *Macromolecules* **2001**, *34*, 795−800.
(14) Schmalz, H.; Abetz, V.; Lange, R. *Compos. Sci. Technol.* **2003**, *63*, 1179−1186.
(15) El Fray, M.; Altstädt, V. *Polymer* **2003**, *44*, 4635−4642.
(16) El Fray, M.; Altstädt, V. *Polymer* **2003**, *44*, 4643−4650.
(17) Le, H. H.; Lüpke, Th.; Pham, T.; Radusch, H.-J. *Polymer* **2003**, *44*, 4589−4597.
(18) Tong, J. D.; Leclère, Ph.; Brédas, J. L.; Lazzaroni, R.; Jérôme, R. *Macromolecules* **2000**, *33*, 470−479.
(19) Arnal, M. L.; Balsamo, V.; López-Carrasquero, F.; Contreras, J.; Carrillo, M.; Schmalz, H.; Abetz, V.; Laredo, E.; Müller, A. J. *Macromolecules* **2001**, *34*, 7973−7982.
(20) Drzal, P. L.; Shull, K. R. *Macromolecules* **2003**, *36*, 2000−2008.
(21) Kwee, T.; Taylor, S. J.; Mauritz, K. A.; Storey, R. F. *Polymer* **2005**, *46*, 4480−4491.
(22) Indukuri, K. K.; Lesser, A. J. *Polymer* **2005**, *46*, 7218−7229.
(23) Curgul, S.; Yilgor, I.; Yilgor, E.; Erman, B.; Cakmak, M.; *Macromolecules* **2004**, *37*, 8676−8685.
(24) Inoue, T.; Moritani, M.; Hashimoto, T.; Kawai, H. *Macromolecules* **1971**, *4*, 500−507.
(25) Qi, H. J.; Boyce, M. C. *Mech. Mater.* **2005**, *37*, 817−839.
(26) Holden, G.; Kricheldorf, H. R.; Quirk, R. P. *Thermoplastic Elastomers*; Hanser Publishers: Munich, 2004.
(27) Ruzette, A.-V.; Leibler, L. *Nat. Mater.* **2005**, *4*, 19−31.
(28) Epps, T. H.; Cochran, E. W.; Hardy, C. M.; Bailey, T. S.; Waletzko, R. S.; Bates, F. S. *Macromolecules* **2004**, *37*, 7085−7088.
(29) Adhikari, R.; Michler, G. H. *Prog. Polym. Sci.* **2004**, *29*, 949−986.
(30) Chapter V of ref 26.
(31) Alexander, S. *Phys. Rep.* **1998**, *296*, 65−236.
(32) Ferry, J. D. *Viscoelastic Properties of Polymers*; Wiley: New York, 1980.
(33) Weiner, J. H. *Statistical Mechanics of Elasticity*; Wiley: New York, 1983.
(34) Bastide, J.; Leibler, L. *Macromolecules* **1988**, *21*, 2647−2649.
(35) Bastide, J.; Leibler, L.; Prost, J. *Macromolecules* **1990**, *23*, 1821−1825.
(36) Rubinstein, M.; Leibler, L.; Bastide, J. *Phys. Rev. Lett.* **1992**, *68*, 405−407.
(37) Rouf, C.; Bastide, J.; Pujol, J. M.; Schosseler, F.; Munch, J. P. *Phys. Rev. Lett.* **1994**, *73*, 830−833.
(38) Ramzi, A.; Zielinski, F.; Bastide, J.; Boué, F. *Macromolecules* **1995**, *28*, 3570−3587.
(39) Ramzi, A.; Hakiki, A.; Bastide, J.; Boué, F. *Macromolecules* **1997**, *30*, 2963−2977.
(40) Westermann, S.; Pyckout-Hintzen, W.; Richter, D.; Straube, E.; Egelhaaf, S.; May, R. *Macromolecules* **2001**, *34*, 2186−2194.
(41) de Gennes, P.-G. *J. Phys. Lett.* **1976**, *37*, L1−L2.
(42) Feng, S.; Sen, P. N. *Phys. Rev. Lett.* **1984**, *52*, 216−219.
(43) Kantor Y.; Webman, I. *Phys. Rev. Lett.* **1984**, *52*, 1891−1894.
(44) Arbabi, S.; Sahimi, M. *Phys. Rev. Lett.* **1990**, *65*, 725−728.
(45) Kellomäki, M.; Aström, J.; Timonen, J. *Phys. Rev. Lett.* **1996**, *77*, 2730−2733.
(46) Farago, O.; Kantor, Y. *Europhys. Lett.* **2000**, *52* 413−419.
(47) Rubinstein, M.; Panyukov, S. *Macromolecules* **1997**, *30*, 8036−8044.
(48) Rubinstein, M.; Panyukov, S. *Macromolecules* **2002**, *35*, 6670−6686.
(49) DiDonna, B. A.; Lubesnky, T. C. *Phys. Rev. E* **2005**, *72*, 066619−066623.
(50) Long, D.; Sotta, P. *IMA Volume in Mathematics and its Applications: Modeling of Soft Matter*; Calderer, M.-C. T., Terentjev, E. M., Eds.; Springer: New York, 2005; Vol. 141, pp 205−234.
(51) Gao, J.; Weiner, J. H. *Macromolecules* **1987**, *20*, 2520−2525.
(52) Gao, J.; Weiner, J. H. *Macromolecules* **1987**, *20*, 2525−2531.
(53) Oberdisse, J.; Ianniruberto, G.; Greco, F.; Marrucci, G. *Europhys. Lett.* **2002**, *58*, 530−536.
(54) Lusignan, C. P.; Mourey, T. H.; Wilson, J. C.; Colby, R. H. *Phys. Rev. E* **1999**, *60*, 5657−5669.
(55) Gasilova, E.; Benyahia, L.; Durand, D.; Nicolai, T. *Macromolecules* **2002**, *35*, 141−150.
(56) Pütz, M.; Kremer, K.; Everaers, R. *Phys. Rev. Lett.* **2000**, *84* 298−301.
(57) Matsuo, E. S.; Orkisz, M.; Sun, S.-T.; Li, Y.; Tanaka, T. *Macromolecules* **1994**, *27*, 6791−6796.
(58) Panyukov, S.; Rabin, Y. *Macromolecules* **1996**, *29*, 7960−7975.
(59) Westermann, S.; Kreitschmann, M.; Pyckout-Hintzen, W.; Richter, D.; Straube, E.; Farago, B.; Goerigk, G. *Macromolecules* **1999**, *32*, 5793−5802.
(60) Wang, M. J. *Rubber Chem. Technol.* **1998**, *71*, 520−589.
(61) Kaufmann, S.; Slichter, W. P.; Davis, D. D. *J. Polym. Sci., Part A2* **1971**, *9*, 829−839.
(62) Haidar, B.; Salah Deradji, H.; Vidal, A.; Papirer, E. *Macromol. Symp.* **1996**, *108*, 147−161.
(63) Tsagaropoulos, G.; Eisenberg, A. *Macromolecules* **1995**, *28*, 6067−6077.
(64) Struik, L. C. E. *Polymer* **1987**, *28*, 1521−1533.
(65) Berriot, J.; Montès, H.; Lequeux, F.; Long, D.; Sotta, P. *Macromolecules* **2002**, *35*, 9756−9762
(66) Berriot, J.; Montès, H.; Lequeux, F.; Long, D.; Sotta, P. *Europhys. Lett.* **2003**, *64*, 50−56.

(67) Montès, H.; Lequeux, F.; Berriot, J. *Macromolecules* **2003**, *36*, 8107−8118.
(68) Gusev, A. A. *Phys. Rev. Lett.* **2004**, *93*, 0304302−0304304.
(69) Starr, F. W.; Schroder, B. T.; Glotzer, S. C. *Macromolecules* **2002**, *35*, 4481−4492.
(70) Doi, M.; Edwards, S. F. *The Theory of Polymers Dynamics*; Clarendon Press: Oxford, U.K., 1986.
(71) *Numerical Recipes in C, The Art of Scientific Computing*, Cambridge University Press: New York, 1992.
(72) Curro, J. G.; Pincus, P. *Macromolecules* **1983**, *16*, 559−562.
(73) Landau, L. D.; Lifshitz, E. M. *Elasticity*; Pergamon Press: New York, 1993.

MA061306E